CALCULATION OF THE SHIELDING EFFECTIVENESS OF CARBON-FIBER COMPOSITE STRUCTURES

Mohammadali Ansarizadeh

A Thesis
in
The Department
of
Electrical and Computer Engineering

Presented in Partial Fulfillment of the Requirements
for the Degree of Master of Applied Science
Concordia University
Montreal, Quebec, Canada

September 2013

CONCORDIA UNIVERSITY
SCHOOL OF GRADUATE STUDIES

This is to certify that the thesis prepared

By: Mohammadali Ansarizadeh

Entitled: "Calculation of the Shielding Effectiveness of Carbon-Fiber Composite Structures"

and submitted in partial fulfillment of the requirements for the degree of

Master of Applied Science

Complies with the regulations of this University and meets the accepted standards with respect to originality and quality.

Signed by the final examining committee:

_____ Chair
Dr. M. Z. Kabir

_____ Examiner, External
Dr. J. Laurin To the Program

_____ Examiner
Dr. C. Trueman

_____ Supervisor
Dr. R. Paknys

Approved by: _____
Dr. W. E. Lynch, Chair
Department of Electrical and Computer Engineering

SEP 11 2013

20____

_____
Dr. C. Mulligan
Associate Dean, Faculty of
Engineering and Computer Science

Abstract

Calculation of the Shielding Effectiveness of Carbon-Fiber Composite Structures

Mohammadali Ansarizadeh

Carbon-fiber composite (CFC) materials are replacing metals in the construction of modern aircraft because of their outstanding strength/weight ratio. The purpose of this thesis is to identify the capabilities and limitations of the commercially available software in calculating the shielding effectiveness (SE) of CFC structures. This work is started by a literature survey focused on the characterization and modeling of CFC panels.

The homogenized model of CFC panels is analyzed using the skin-effect approximation in a method of moments (MoM) solution. It is found that the stack-to-sheet conversion is a limiting factor in the skin effect approximation and not the homogenization scheme.

Experimental results are presented which indicate that performance of monopole antennas up to a frequency of 12.5 GHz is not altered by replacing a metallic ground plane with a CFC one. Also, a monopole antenna is mounted on hollow CFC and aluminum cubes with the same physical dimensions and the radiated electromagnetic interference (EMI) inside the cube are theoretically compared.

Although wire meshes with unbonded junctions are better shields it is shown that this is less important for meshes is epoxy as compared to free space. For CFC materials reinforced with woven carbon-fiber fabrics the effects of physical contact between orthogonally oriented fiber bundles are examined. It is found that bonding CFC fiber bundles at the junctions actually improves the shielding performance.

The simulation results for the electric and magnetic SE inside a hollow spherical CFC shell are compared with the benchmark analytic solutions. It is shown that the analytic solutions could not be numerically evaluated unless the wave functions are

expressed in terms of the thickness of CFC materials.

Acknowledgements

I would like to thank my supervisor Prof. Robert Paknys for his academic and financial support. This work would not have been possible without his support and supervision. I am grateful to Prof. Sebak and Dr. Alper Ozturk for their supervision in the early stages of my research. I appreciate Prof. Laurin for providing me access with the measurement setup at École Polytechnique de Montréal and, also, valuable feedback about my work. I thank Prof. Kishk for answering some of my questions.

Support from the National Science and Engineering Research Council (NSERC) CRD Program, the Consortium de Recherche et d'Innovation en Aerospatiale au Québec (CRIAQ) and industry partners Bombardier Aerospace and MacDonald Dettwiler and Associates Inc. is gratefully acknowledged.

I appreciate Shailesh Prasad, Dr. Donald Davis and my good friends and colleagues Ali Chakavak, Ayman, Zouhair, Tiago Leao, Mohamed Hassan, and Mehdi Ardavan. Last but not least, I thank my parents for their support and sacrifices.

Contents

List of Figures

List of Symbols and Acronyms

β_0	Propagation constant in free space
δ_s	Skin depth
ϵ_0	Permittivity of free space
ϵ_m	Permittivity of epoxy
ϵ_r	Relative permittivity
η_0	Impedance of free space
λ	Material wavelength
μ_0	Permeability of free space
σ	Conductivity
c_0	Speed of light in free space
k_0	Wavenumber in free space
Z_s	Equivalent sheet impedance
$\mathbf{J}_s$	Equivalent electric surface current
$\mathbf{E}$	Electric field
$\mathbf{H}$	Magnetic field
CFC	Carbon-Fiber Composite

EM Electromagnetics

EMC Electromagnetic Compatibility

EMI Electromagnetic Interference

FEKO *FEldberechnung bei Körpern mit beliebiger Oberfläche*, meaning, Field computations involving bodies of arbitrary shape

FIT Finite Integration Technique

HFSS High Frequency Structural Simulator

MoM Method of Moments

PEC Perfect Electric Conductor

PMCHWT Poggio Miller Chang Harrington Wu Tsai

RCS Radar Cross Section

SE Shielding Effectiveness

SEL Segment Edge Length

SEP Surface Equivalence Principle

SIE Surface Integral Equations

TEL Triangle Edge Length

UHF Ultra High Frequency

VEP Volume Equivalence Principle

VHF Very High Frequency

Chapter 1

Literature Survey

1.1 Introduction

There is a growing trend in the aerospace industries to replace metals with carbon-fiber composite (CFC) materials because they offer superior mechanical performances at a lower cost [6]. In fact, the Bombardier aerospace company is using CFC materials in the construction of its modern aircraft. CFC panels are synthesized as a sandwich of multiple laminates. A laminate is often composed of a planar array of long continuous carbon-fibers embedded in an epoxy host medium. A single laminate is strongly anisotropic. However, by progressively changing the orientation of the reinforcing carbon-fibers in a CFC panel, bulk isotropic mechanical and electrical material properties may be obtained. The anisotropic conductivity of a single CFC laminate is not of interest in this thesis because CFC panels with industrial applications are usually quasi-isotropic which are modeled as isotropic conducting materials with a conductivity in the order of 10^4 S/m [7]. In fact, the conductivity of CFC materials is almost 1000 times lower than the conductivity of most metals. Since conductivity plays an important role in SE, the EMC may be compromised by replacing metals with CFC materials. Therefore, it is necessary to understand the capabilities and limitations of the commercially available software while calculating

the SE of CFC structures so that the design engineer can assure if a CFC substitute will meet the required standards. FEKO offers a MoM solver for SE problems involving CFC materials. The purpose of this thesis is to understand the capabilities and limitations of an MoM SIE formulation in calculating the SE of CFC structures. This formulation is conveniently available in the commercial EM solver code FEKO [8].

To understand the research history on the EM properties of CFC materials, a brief literature survey on characterization and modeling of CFC materials is presented in the following section.

1.2 Overview of the Pioneering Research

To our knowledge, the earliest EM study of CFC materials dates back to 1971 which was focused on the homogenized conductivity of a single laminate [9]. Later in 1972, a series of destructive and nondestructive experiments focused on the effects of lightning-produced currents on CFC panels were reported [10]. Knibbs and Morris modeled a CFC laminate from the knowledge of its mechanical, thermal, and electrical properties [11]. Their model was based on fibers embedded in a dielectric host medium. It was concluded that fibers in a CFC laminate do not have exactly the same orientation and there is misalignment from the nominal orientation. Moreover, there are fiber-to-fiber electrical contacts in a laminate which are only 25% effective [11]. In 1975, Keen tested a CFC reflector antenna and reported that at X-band frequencies if the surface of a CFC reflector is not covered with a metallic coating then a gain loss of 0.5 dB is incurred [12]. Later, Keen pointed out that the surface roughness is the main cause of the gain loss and not the relatively lower conductivity of CFC materials [13]. According to Blake, the difference between the gain and radiation pattern of UHF antennas mounted on metallic and CFC ground planes is "little". However, the magnetic SE of CFC materials is reported as "minimal" [14].

Casey in 1977, calculated the SE of CFC panels by using boundary conditions that relate the tangential electric and magnetic fields on both sides of a laminate [15]. Casey noted that quasi-isotropic CFC panels can be modeled as isotropic conducting materials with a conductivity in the order of 10^4 S/m. Weinstock studied the impact of replacing metals with CFC panels in the construction of aircraft [16]. One of his conclusions was that the main reasons for the reduction of SE in CFC enclosures are the discontinuity of the surface currents at seams and joints.

Hill and Wait calculated the reflection and transmission coefficients of wire meshes in free space and reported that unbonded wire meshes are superior EM shields compared to the bonded case [17]. Holloway *et al.* proposed equivalent-layer models to simplify analysis of CFC panels [1]. In their model, the electrical contact between fibers in the same laminate or in adjacent laminates were ignored. Kazerani used FEKO to obtain the radiation pattern of antennas that are mounted on a CFC aircraft fuselage [18]. Mehdipour used the equivalent-layer models of Holloway *et al.* to calculate the SE of CFC materials [19]. Furthermore, Mehdipour *et al.* showed that carbon-fiber nanotubes may be used to increase the conductivity of CFC materials [20].

Due to a limited current handling capability, CFC materials are damaged by high electric currents associated with lightning strikes. Therefore, a series of lighting protection schemes for CFC materials have been developed [21].

1.3 Basic Assumptions

This work is focused on calculating the SE of CFC structures using the commercially available software FEKO [8]. We will focus on the surface integral equations (SIE) and method of moments (MoM) solver in FEKO. Throughout this thesis, the term "CFC laminate" is referred to a dielectric slab reinforced with long continuous parallel carbon-fiber reinforcements. If there is only one laminate then the reinforcing fibers

are equally spaced and non-touching but in practice not all fibers are parallel and there is misalignment between the fibers. Moreover, there is electrical contact between the reinforcing fibers in a CFC panel. The term "panel" refers to a material whose width and length are much larger than its thickness. The term "CFC panel" refers to the sandwich structure of woven fibers forming multiple CFC laminates. In this thesis, CFC panels with quasi-isotropic material properties are modeled as isotropic conducting materials with $\sigma = 10^4$ S/m unless otherwise stated [22]. Furthermore, simulation or analytic results that differ by less than 3 dB are considered to be in good agreement with one another.

1.4 Thesis Outline

The thesis is organized as follows. In Chapter 2, the skin-effect approximation is used in a MoM solver to calculate the reflection and transmission coefficients of CFC panels and the results are compared with Holloway *et al.* [1]. Application of the skin-effect model is motivated by a FEKO application note in which CFC panels were modeled using the skin-effect approximation [23]. In Chapter 3, effects of replacing metallic structures with CFC ones on the reflection coefficient, radiation pattern, or radiated electromagnetic interference (EMI) of monopole antennas are examined. Experimental and simulation results will be reported. This chapter is motivated by the fact that in modern aircraft, monopole antennas are being mounted on a CFC rather than a metallic fuselage. Chapter 4 is focused on the effects of bonding between orthogonally oriented reinforcements in adjacent laminates. The reinforcing fibers in the CFC panels that were analyzed by Holloway *et al.* were unbonded while some CFC panels have a woven structure with physical contact between orthogonally oriented reinforcements. The bonding between orthogonally oriented wires can affect the reflection and transmission coefficient of wire meshes [17, 24, 25, 26]. That is why in Chapter 4, effects of interlaminar bondings on the reflection and transmission

coefficients of CFC panels are investigated. Chapter 5 is focused on the electric and magnetic SE of CFC enclosures. Certain benchmark solutions are developed to validate the FEKO simulation results. Numerical difficulties were encountered while evaluating the benchmark SE quantities. In Appendix A, an approach is presented to resolve such numerical problems. Finally, conclusions and suggestions for future work are presented in Chapter 6.

Chapter 2

The Skin-Effect Approximation

2.1 Introduction

An ideal model of a CFC laminate is a dielectric slab reinforced by an array of long continuous carbon-fibers. In each laminate, carbon-fibers are assumed to be parallel, equally spaced, and not in contact with one another. CFC panels are usually composed of a stack of multiple laminates where in each laminate carbon-fibers have a specific orientation. By changing the orientation of the reinforcing fibers through the panel, quasi-isotropic mechanical and electrical properties are obtained. The diameter of individual carbon-fibers and the spacing between the fibers are in the order of micrometers. However, frequency bands that are used in navigation and communication systems correspond to wavelengths that are much larger than the geometrical periodicity of CFC materials. As a result, CFC panels can be replaced with equivalent homogeneous models because it is not necessary to calculate surface or volume currents for individual carbon-fibers. Consequently, the EM analyses of CFC materials is greatly simplified.

In order to analyze CFC materials in FEKO it is recommended that the skin-effect model ("SK-card") be used [23]. This approach is motivated by a FEKO application note in which the skin-effect model is used to calculate the RCS of aircraft with a

CFC skin [23, 27]. The FEKO skin-effect model is based on approximate boundary conditions and calculates the electric surface currents on CFC materials. The FEKO skin-effect model can be used to analyze CFC panels composed of a single or multiple laminates. The main purpose of this chapter is to examine FEKO's ability to calculate the EM SE of CFC panels. The geometrical and constitutive parameters of the panels under consideration are the same as those used by Holloway *et al.* so that a comparison can be made between published results and FEKO simulations.

This chapter is organized as follows. In the next section, a CFC laminate is modeled with an equivalent-layer model composed of three homogeneous layers. Calculation of the homogenized complex tensor permittivity of fibers embedded in a dielectric slab is discussed in Section 2.3. In Section 2.4, the skin-effect approximation in FEKO is briefly explained. Then in Section 2.5, the multilayer structure CFC panels is shrunk to a sheet with zero thickness. Next in Section 2.6, the simulation results for the reflection and transmission coefficients of CFC panels composed of one, two, and four laminates are presented and compared with published literature [1]. Moreover, the magnetic SE at the center of a hollow cubic shell with a CFC face is calculated using the skin-effect model and results are compared with published literature [2]. Finally, conclusions are made in Section 2.7.

2.2 Homogenization of a CFC Laminate

Figs. 2.1a and 2.1b show the idealized model of a CFC laminate and its equivalent layer model, respectively. With reference to Fig. 2.1a, D is the fiber diameter, P is periodicity of the reinforcing fiber array, and L is the laminate thickness. The model shown in Fig. 2.1a can be analyzed using one unit cell and application of the periodic boundary conditions. But since the physical spacing between the reinforcing carbon-fibers is usually much smaller than the wavelength of the excitation signals it is possible to replace all the fibers embedded in the binding dielectric material

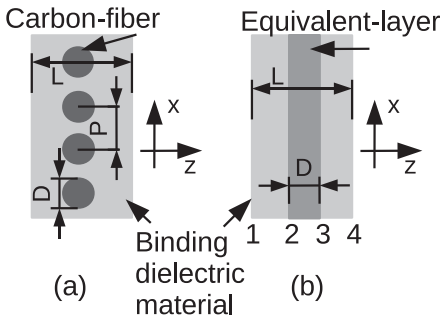

Figure 2.1: (a) and (b) are, respectively, the idealized geometry of a CFC laminate and its equivalent layer model [1].

with a homogeneous slab. The equivalent-layer model which is shown in Fig. 2.1b is comprised of three homogeneous layers [1]. The left and right layers are slabs of the binding dielectric material with a thickness of $(L - D)/2$. The fibers embedded in the binding material are replaced by an anisotropic layer of thickness D. When the equivalent-layer model is applied to a CFC panel comprised of n-laminates then the final model will be composed of 2n+1 layers. Each layer is homogeneous but can be anisotropic. The equivalent-layer model is well suited to the skin-effect model.

2.3 Tensor Permittivity of Embedded Fibers

In order to apply the skin-effect approximation to a CFC laminate the equivalent tensor permittivity and conductivity of the middle layer shown in Fig. 2.1b must first be calculated. The equivalent tensor permittivity and conductivity of embedded fibers are obtained from the geometrical and electrical properties of the binding dielectric material and reinforcing fibers. Let $(\epsilon_{||},\ \epsilon_{\perp})$ and $(\sigma_{||},\ \sigma_{\perp})$ denote the homogenized equivalent permittivity and conductivity parallel and orthogonal to the fibers in the plane of the laminate. To calculate $\epsilon_{||}$, $\epsilon_{\perp}$, $\sigma_{||}$, and $\sigma_{\perp}$, Holloway *et al.* used

$$\epsilon_{||} - j\frac{\sigma_{||}}{\omega} = (1-g)\epsilon_m + g(\epsilon_f - j\frac{\sigma_f}{\omega}) \tag{2.1}$$

and

$$\left[\epsilon_{\perp} - j\frac{\sigma_{\perp}}{\omega}\right]^{-1} = (1-g){\epsilon_m}^{-1} + g(\epsilon_f - j\frac{\sigma_f}{\omega})^{-1} \tag{2.2}$$

where ϵ_m and ϵ_f are, respectively, the permittivity of the binding material and carbon-fibers. σ_f is the conductivity of the fibers and the conductivity of the binding dielectric material is assumed to be zero. Moreover, g is called the "volume fraction" of carbon-fibers and is given by [1]

$$g = \frac{\pi D}{4P} \ . \tag{2.3}$$

Material properties in the direction normal to the CFC laminate are not required when using the skin-effect approximation because the laminate will be shrunk to a sheet with zero thickness. In fact, the VEP currents normal to the plane of a CFC laminate are ignored in the skin-effect approximation.

Now two dielectric materials should be created in FEKO with ($\epsilon_{||}$, $\sigma_{||}$) and ($\epsilon_{\perp}$, $\sigma_{\perp}$) corresponding to the material properties along and orthogonal to the fibers orientation. In the next section application of the skin effect approximation to a dielectric slab is explained.

2.4 The Skin-Effect Approximation

Although the homogenization technique discussed in Section 2.2 greatly facilitates simulation of the CFC laminate shown in Fig. 2.1a it is possible to further simplify the equivalent-layer model shown in Fig. 2.1b. The typical thickness of a CFC laminate is in the order of L=0.13 mm [28, 29]. If the tangential electric field is approximately the same through the laminate then it is not necessary to calculate electric and magnetic surface currents on the four boundaries in Fig. 2.1b. Since CFC materials are not magnetic it is possible to replace the equivalent-layer model shown in Fig. 2.1b with electric surface currents on a sheet. In fact, in the skin-effect approximation the VEP currents are converted to surface currents provided that the panel thickness is thin with respect to the material wavelength i.e., $|\gamma L| < 0.2$ where

γ is the propagation constant in the laminate and L is the panel thickness [30].

A surface which supports an electric surface current such that $\mathbf{E}_{tan} = Z_s\mathbf{J}_s$ is called an "impedance sheet" and Z_s is referred to as the "sheet impedance". For a thin dielectric slab with a thickness of L, conductivity of σ and permittivity of ϵ the equivalent sheet impedance is given by [31, 32]

$$Z_s = \frac{\beta}{2(\sigma + j\omega\epsilon - j\omega\epsilon_e)\sin(\frac{\beta L}{2})} \tag{2.4}$$

where $\beta = \omega\sqrt{\mu_0(\epsilon + \sigma/j\omega)}$ is the propagation constant in the dielectric material and ϵ_e is the permittivity of the background medium. For lossless media $\sigma = 0$, ϵ and ϵ_e are real and Z_s will also be real. However, for lossy media $\sigma \neq 0$ and β and Z_s are complex quantities. For an array of carbon-fibers embedded in a binding dielectric material, Eqs. 2.1 and 2.2 are used to calculate the equivalent sheet impedance along the laminate's principal directions.

For the equivalent-layer model shown in Fig. 2.1b, FEKO recognizes three sheet impedances corresponding to the three dielectric layers. In the next section, the three impedance sheets will be merged into one sheet.

2.5 Stack-to-Sheet Conversion

There is usually more than one laminate in a CFC panel and the orientation of the reinforcing fibers varies through the panel. Let $\bar{\bar{Z}}_{si}^{L}$ represent the tensor sheet impedance of the i-th laminate of a CFC panel with N laminates. Furthermore, let Z_{sdi} represent the sheet impedance of the left and right dielectric layers in the equivalent-layer model of the i-th laminate. Finally, let $Z_{s||i}$ and $Z_{s\perp i}$ denote the sheet impedance of the middle layer in the equivalent-layer model of the i-th laminate.

Then, $\bar{\bar{Z}}_{si}^{L}$ is written as:

$$\bar{\bar{Z}}_{si}^{L} = \left\{ \begin{bmatrix} Z_{sdi} & 0 \\ 0 & Z_{sdi} \end{bmatrix}^{-1} + \begin{bmatrix} Z_{s\|i} & 0 \\ 0 & Z_{s\perp i} \end{bmatrix}^{-1} + \begin{bmatrix} Z_{sdi} & 0 \\ 0 & Z_{sdi} \end{bmatrix}^{-1} \right\}^{-1} . \tag{2.5}$$

$\bar{\bar{Z}}_{si}^{L}$ is defined in a local coordinate system associated with the i-th laminate. In order to describe the tensor sheet impedance of the i-th laminate in the panel's coordinate system the following transformation is used

$$\bar{\bar{Z}}_{si}^{P} = \bar{\bar{T}}_i \bar{\bar{Z}}_{si}^{L} \bar{\bar{T}}_i^{-1} \tag{2.6}$$

where

$$\bar{\bar{T}}_i = \begin{bmatrix} \cos\alpha_i & -\sin\alpha_i \\ \sin\alpha_i & \cos\alpha_i \end{bmatrix} \tag{2.7}$$

and α_i is the angle that the fibers in the i-th laminate make with the panel's reference direction [32]. Finally, the tensor sheet impedance of a CFC panel with N laminates in the panel's coordinate system can be written as [31]:

$$\bar{\bar{Z}}_s = \left[\sum_{i=1}^{N} \bar{\bar{Z}}_{si}^{P^{-1}} \right]^{-1} . \tag{2.8}$$

The expression of $\bar{\bar{Z}}_s$ is very similar to the overall impedance of multiple shunt loads because it is assumed that the electric field is almost the same through the panel's thickness. In the skin-effect approximation, $\bar{\bar{Z}}_s$ is used to calculate the surface currents that penetrate CFC panels. The surface currents on a CFC panel are found such that they reproduce the scattered fields of the original CFC panel. Using the skin-effect approximation the fields everywhere in space are the summation of the incident and scattered fields.

In the following section, the skin-effect model is used to calculate the reflection and transmission coefficients of infinite CFC panels. Moreover, the magnetic SE inside a hollow cubic shell with a CFC face is also obtained.

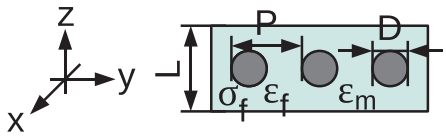

Figure 2.2: The geometry of the ideal model of a CFC laminate. D, P, and L are, respectively, the fiber diameter, periodicity of the fiber array, and laminate thickness. $\epsilon_m = 2\epsilon_0$ is the permittivity of the binding dielectric material. $\epsilon_f = 2\epsilon_0$ and $\sigma_f = 10^4$ S/m are the permittivity and conductivity of the fibers, respectively.

2.6 Numerical Results

2.6.1 A Single CFC Laminate

Fig. 2.2 shows the geometry of a CFC panel with one laminate. With reference to Fig. 2.2, the geometrical and electrical parameters of the laminate are $D = 0.05$ mm, $P = 0.1$ mm, $L = 0.75$ mm, $\epsilon_m = \epsilon_f = 2\epsilon_0$, and $\sigma_f = 10^4$ S/m [1]. The laminate is normally illuminated by a plane wave which may be polarized parallel or orthogonal to the reinforcing fibers. Eqs. (2.1) and (2.2) are used to calculate the homogenized constitutive parameters of the middle layer in the equivalent-layer model. As a result, $\epsilon_{||} = 2\epsilon_0$ and $\sigma_{||} = 3927$ S/m in the direction parallel to fibers. The constitutive parameters in the direction orthogonal to the fibers are $\epsilon_\perp = 3.3\epsilon_0$ and $\sigma_\perp \approx 0$ S/m. Fig. 2.3 shows a good agreement between the skin-effect model (FEKO-SK), FEM solution of Holloway *et al.*, and FEM solutions of HFSS for $|\Gamma_{||}|$ and $|\Gamma_\perp|$ [1, 33]. The subscripts $_{||}$ and $_\perp$ indicate that the incident plane is polarized parallel or orthogonal to the fibers. The FEM results correspond to the full wave simulations of the exact geometry of the laminate. Holloway *et al.* did not report $|T_{||}|$ or $|T_\perp|$ in [1]. Therefore, HFSS simulation results are provided. Fig. 2.3 confirms that the homogenization method discussed in Section 2.2 along with the skin-effect approximation in FEKO can be used to obtain the reflection and transmission coefficients of a CFC laminate. Fig. 2.3 shows that when the incident electric field is polarized parallel to the fibers then the laminate acts as a metallic slab because $|\Gamma_{||}| \approx 0$ dB and $|T_{||}| \approx -31.5$ dB.

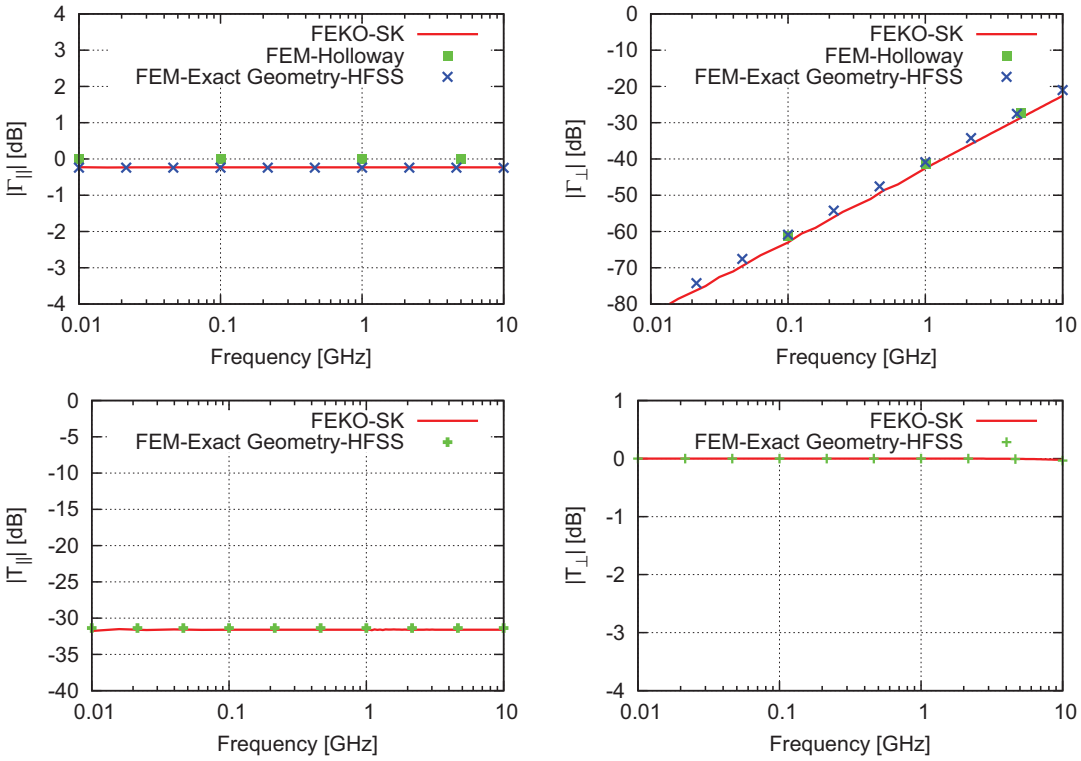

Figure 2.3: The reflection and transmission coefficients of the CFC laminate shown in Fig. 2.2. A comparison is made between the skin-effect model and FEM solutions reported by Holloway or obtained using HFSS. The subscripts $_{||}$ and $_{\perp}$ indicate that the incident plane wave is polarized parallel or orthogonal to the fibers.

However, if the incident electric field is polarized orthogonal to the fibers then the laminate acts as a thin dielectric slab because $|T_{\perp}| \approx 0$ dB. In the following section, the skin-effect model is applied to a CFC panel with two laminates.

2.6.2 CFC Panel with Two Laminates

Fig. 2.4 shows the geometry of an infinite CFC panel comprised of two laminates. The geometrical structure and electrical properties of each laminate are the same as those given in Section 2.6.1. The reinforcing fibers in the two laminates are oriented orthogonal to one another. The panel is illuminated by $\mathbf{E}^i_{||} = \hat{\mathbf{y}} e^{jk_0 z}$ or $\mathbf{E}^i_{\perp} = \hat{\mathbf{x}} e^{jk_0 z}$ where k_0 is the wavenumber of the incident plane wave in free space. The subscripts $_{||}$ and $_{\perp}$ indicate that the incident plane wave is polarized parallel or orthogonal to

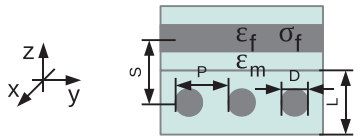

Figure 2.4: The geometry of a CFC panel with two laminates. The reinforcing fibers are oriented along the y- and x-axis. The geometrical and electrical parameters of each laminate are given in Section 2.6.1.

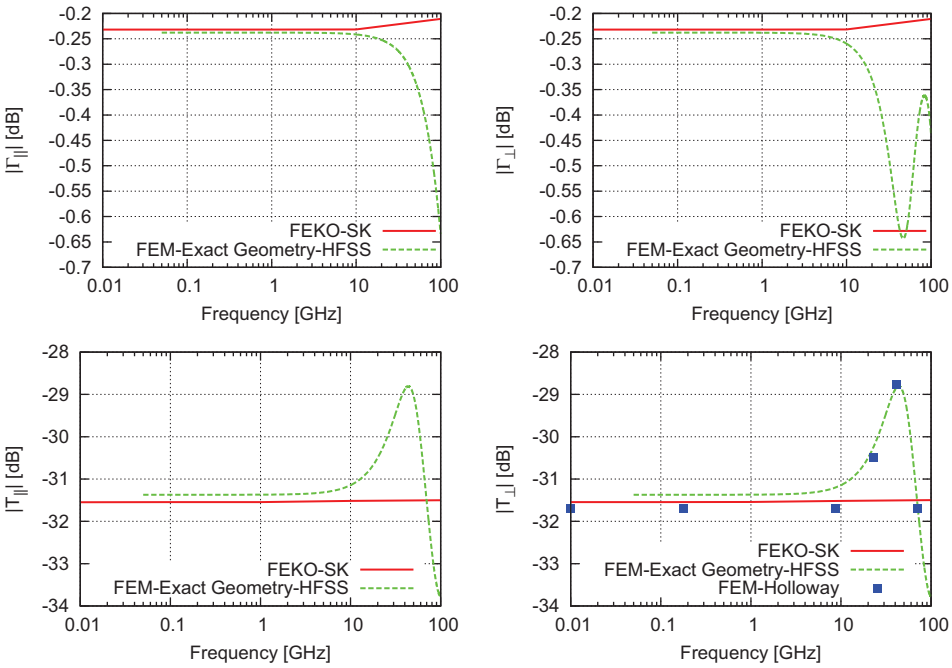

Figure 2.5: The reflection and transmission coefficients of a CFC panel with two laminates for a normally incident plane wave. The panel is illuminated by a normally incident plane wave polarized along the x- and y-axis.

the fibers oriented along the y-axis. Using the homogenization method discussed in Section 2.2, the equivalent-layer model of each laminate is obtained and fed to the skin-effect model in FEKO. Then, the reflection and transmission coefficients of the panel are obtained using double periodic boundary conditions and simulation results are shown in Fig. 2.5. The MoM solutions of the skin-effect model (FEKO-SK) are compared with FEM solutions reported by Holloway *et al.* or obtained using HFSS simulations [1]. The FEM solutions correspond to the full wave analysis of the unit cell of the panel shown in Fig. 2.4. Holloway's solutions were available only for $|T_{\perp}|$ [1].

Hence, HFSS simulation results are also presented. Fig. 2.5 shows that having fibers oriented in two orthogonal orientations eliminated the strong anisotropic behavior of a single CFC laminate. The magnitude of the reflection coefficients $|\Gamma_{||}|$ or $|\Gamma_{\perp}|$ is almost 0 dB indicating that the incident plane wave is reflected and not absorbed by the panel. Moreover, for $f \leq 10$ GHz the tangential electric field is almost the same through the panel's thickness and $|T_{||}| \approx |T_{\perp}| \approx -31.5$ dB. In Section 2.6.1, $|T_{||}| \approx -31.5$ dB for a single laminate. It is evident that the laminate in which fibers are oriented orthogonal to the polarization of the incident plane wave does not contribute in the SE. It is worth noting that since $|\Gamma_{||}|$ and $|\Gamma_{\perp}|$ are almost 0 dB they are not sensitive to the approximations that are made in the skin effect model. However, Fig. 2.5 reveals that the skin-effect model has limitations in SE calculations because the FEKO-SK solution for $|T_{||}|$ and $|T_{\perp}|$ start to deviate from the exact solutions for $f > 10$ GHz.

For a homogeneous conducting panel the SE is due to reflection and absorption [4]. The FEKO skin-effect model is capable of modeling only the reflection portion of the shielding mechanism because the skin-effect approximation neglects the variations of the electric field as the wave travels through the lossy material. Absorption loss is about 1 dB when the material is one skin-depth thick. This is also the point at which the skin-effect approximation begins to deteriorate. Therefore, as the panel's physical thickness increases the highest frequency at which the skin-effect model can be used in SE calculations decreases. FEKO does not yet have the capability of using the ABCD parameters of each laminate of a CFC panel to eliminate such limitations on the panel's thickness. To further elaborate this point, a CFC panel with four laminates is simulated in the next section.

2.6.3 CFC Panel with Four Laminates

Fig. 2.6 shows the geometry of a CFC panel composed of four laminates. The reinforcing fibers are oriented as 0/90/0/90 degrees with respect to the y-axis. The laminates

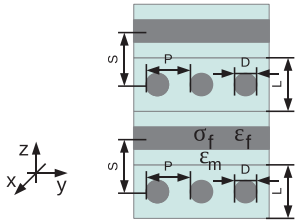

Figure 2.6: The geometry of a CFC panel comprised of four laminates. The laminates have the same geometrical and electrical properties as the one discussed in Section 2.6.1.

have the same geometrical and electrical properties as the laminate discussed in Section 2.6.1. Moreover, the panel is illuminated by a normally incident plane wave which may be polarized along $\hat{\mathbf{y}}$ ($||$) or $\hat{\mathbf{x}}$ ($\perp$). The equivalent-layer model of the panel is composed of nine homogeneous layers where five layers are isotropic and four anisotropic. The isotropic layers are made of the binding dielectric material and the anisotropic layers are specified in Section 2.6.1. Fig. 2.7 shows the simulation results for the reflection and transmission coefficients of the panel. A comparison is made between the MoM solution to the panel's skin-effect model (FEKO-SK), FEM solution for the panel's exact geometry, and the FEM solution for the panel's equivalent-layer model (FEM-ELM) without using the skin-effect approximation [1]. FEM solutions reported by Holloway *et al.* are, also, presented.

Fig. 2.7 shows a good agreement between the FEKO skin-effect and exact models for $f \leq 0.4$ GHz. It is observed that for $f \leq 0.4$ GHz, we have $|T_{||}| \approx |T_{\perp}| \approx -37$ dB or SE=37 dB which shows 5.5 dB increase over the panel with two laminates as discussed in the previous section. Fig. 2.7, also, shows that the skin-effect model should not be used to calculate $|T_{||}|$ or $|T_{\perp}|$ for $f > 1$ GHz. However, since $|\Gamma_{||}| \approx |\Gamma_{\perp}| \approx 0$ dB the magnitude of the reflection coefficient is not sensitive to the approximations that are made in the skin-effect model. Thus, when the skin-effect approximation is employed the dB-quantity of error in SE calculations can be much larger compared to those in the reflection coefficient calculations. In fact, application of the FEKO skin-effect model to SE problems is limited by the stack-to-sheet conversion and not

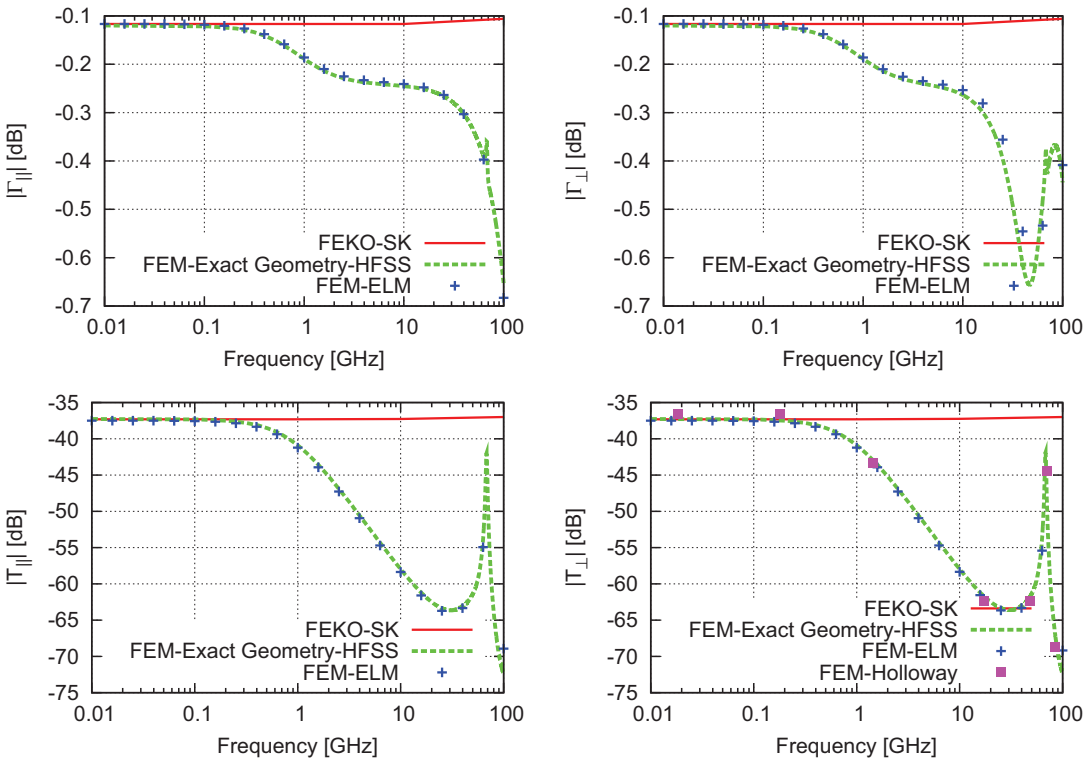

Figure 2.7: The reflection and transmission coefficients of a CFC panel with four laminates. The fibers in the panel are oriented as 0/90/0/90 degrees with respect to the y-axis, as shown in Fig. 2.6. The panel is illuminated by a normally incident plane wave which may be polarized along the y- (||) or x-axis (⊥).

the homogenization method discussed in Section 2.2. To prove this point, the FEM solutions for the panel's equivalent-layer model (FEM-ELM) are shown in Fig. 2.7. The good agreement between the reflection and transmission coefficient of the exact geometry and its equivalent-layer model proves that the stack-to-sheet conversion limits application of the FEKO skin-effect model in SE calculations.

In the next section, the skin-effect model is applied to a finite structure.

2.6.4 Hollow Cubic Shell with a CFC Face

Fig. 2.8a shows a hollow cubic shell with a side length of $W = 0.5$ m. The front face of the shell has a conductivity of $\sigma = 4 \times 10^4$ S/m and thickness of $d = 2$ mm. Other faces of the shell are copper with a conductivity of $\sigma_{Cu} = 5.7 \times 10^7$ S/m and thickness

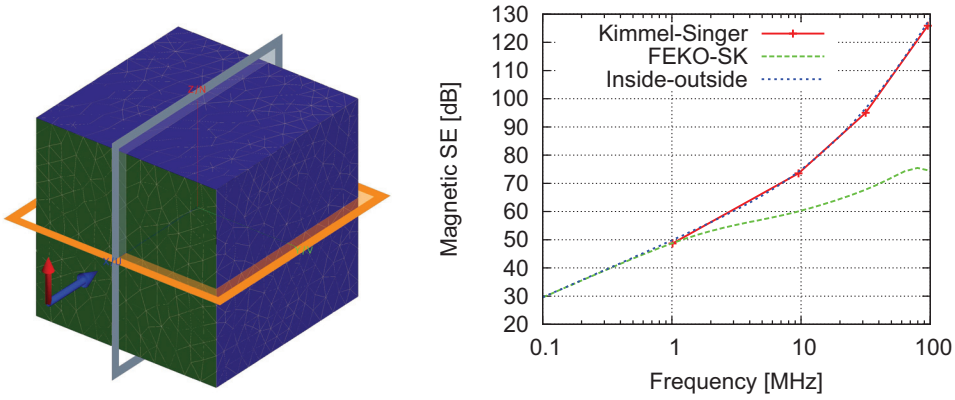

(a) (b)

Figure 2.8: The magnetic SE at the center of a hollow cubic shell with a side length of 0.5 m. All faces of the cube are copper with a thickness of 0.1 mm except for the front face which is CFC with a thickness of 2 mm and conductivity of $\sigma = 4 \times 10^4$ S/m. A comparison is made between the skin-effect model, inside-outside formulation, and results reported by Kimmel and Singer [2].

of 0.1 mm. The CFC face is illuminated by the plane wave $\mathbf{E}^i = 120\pi\hat{\mathbf{z}}e^{jk_0x}$ V/m where $k_0 = 2\pi/\lambda_0$ and λ_0 is the wavelength of the incident plane wave in free space. The electric and magnetic symmetries of the problem with respect to the $z = 0$ and $y = 0$ planes are applied in order to accelerate the simulations. In this section, the magnetic SE at the center of the cube is obtained using two different formulations, the skin-effect model and inside-outside formulation. The inside-outside formulation is the standard approach in FEKO for SE calculations as will be described in Chapter 5. In the skin-effect approximation the simulation results for the SE are sensitive to the discretization errors in the surface currents because inside conducting enclosures the fields produced by the surface currents should almost perfectly cancel the incident fields. In this section, the mesh size is progressively reduced until the simulation results approached a final solution. The inside-outside formulation did not show such dependence on the mesh size. The simulations results for the magnetic SE at the center of the cube i.e., $SE = |\mathbf{H}(0,0,0)|_{no\ cube}/|\mathbf{H}(0,0,0)|_{cube}$ are shown in Fig. 2.8b. The FEKO simulations are performed for a mesh size of $W/10$. The shell is meshed into 946 triangle surface elements. Furthermore, the total number of unknowns are,

respectively, 709 and 1418 in the skin-effect model and inside-outside formulation.

Fig. 2.8b shows very good agreement between the simulation results for the skin-effect approximation and inside-outside formulation for $f \leq 1$ MHz. Because $\sigma_{Cu} \gg \sigma_{CFC}$ the leakage through the copper faces can be ignored compared to the leakage through the CFC face. At $f = 1$ MHz, the thickness of the CFC face is $d = 0.8\delta_s$ and that is where the results of the skin-effect approximation start to deviate from the other solutions as the frequency increases. An excellent agreement is observed between the inside-outside formulation and published results [2]. The thickness of the front face is $d = 8\delta_s$ at $f = 100$ MHz. If the dB-quantity of the SE is small and is basically determined by the presence of apertures, cracks, or seams on the CFC structure and not the leakage through a CFC skin then the skin-effect model might be an efficient tool.

2.7 Conclusions

Using homogenization techniques and the FEKO skin effect model ("SK-card") the reflection and transmission coefficients of CFC panels were obtained and validated. In the skin-effect model, an equivalent tensor sheet impedance was found such that the total electric VEP currents that penetrate a CFC panel are reproduced on an impedance sheet. The skin-effect model used stack-to-sheet conversion approach to shrink CFC panels to an impedance sheet with zero thickness. As a result, the scattered fields produced by CFC panels composed of a single or multiple laminates could be calculated with no more simulation resources than what would be required if the panel was PEC. This is the greatest merit of the skin-effect model especially useful for electrically large structures, such as CFC aircraft. The tensor complex permittivity of each laminate was calculated with homogenization techniques and then used in the skin-effect model. For CFC panels with one, two, and four laminates the FEKO MoM simulation results were compared and validated with published FEM

solutions or those of the HFSS. It was observed that the reflection coefficient of CFC panels was not prone to errors associated with the skin-effect approximation because often $|\Gamma| \approx 0$ dB for CFC panels. The limitation of the skin-effect model in calculating the SE of CFC panels with multiple laminates was shown to be caused by the stack-to-sheet conversion and not homogenization techniques. Moreover, it was observed that the fibers that were oriented orthogonal to the polarization of the incident plane wave did not contribute in the shielding mechanism.

The plane wave magnetic SE at the center of a hollow cubic shell with a CFC face was also calculated using the skin-effect model and the results were compared with published literature and agreement was obtained for $d \leq 0.8\delta_s$. Although the skin-effect model could be used in SE calculations a very fine mesh might have to be used to eliminate discretization errors associated with the representation of the surface currents in terms of the basis functions. This limitation can be overcome with the inside-outside formulation. The skin-effect model is best used for calculating the scattered fields of CFC structures. Moreover, if the SE is determined by apertures, crack, and seams on a CFC structure and not leakage through a CFC material then the skin-effect model might also be useful.

Chapter 3

Monopole Antennas on CFC Structures

3.1 Introduction

A typical aircraft can use as many as 20 antennas for communication, navigation, instrument landing systems, radar altimeter, and other purposes [34]. Therefore, in this chapter, the reflection coefficient and radiation pattern of monopole antennas mounted on metallic and CFC ground planes are experimentally examined [35].

The impact of replacing metals with CFC materials on the EMI inside CFC enclosures is examined in this chapter. The electrical conductivity of a barrier plays a key role in reducing the level of fields that leak into an enclosure and meeting EMC requirements. The conductivity of CFC materials is 1000 times lower than that of most metals [1]. Moreover, the permeability of CFC materials is basically that of the free space. Therefore, the attenuation of EM waves propagating in CFC materials is much lower compared to metals.

The term SE usually refers to the SE to electric fields [4]. The SE to magnetic fields is more dependent on the barrier's conductivity compared to the SE to electric fields. Therefore in this chapter, the leakage of magnetic fields as well as electric fields

Figure 3.1: Monopole antennas mounted on metallic (top view) and CFC (top and bottom views) ground planes.

into enclosures are examined [4].

The skin depth is $1/\sqrt{\pi f \mu_0 \sigma}$ and approximately 32 times larger in CFC materials compared to metals. Therefore, the difference between metallic and CFC shields manifest at frequencies for which the metallic barrier is much thicker than the skin depth in the barrier while a CFC replacement with the same physical thickness is not. The CFC materials that are considered in this chapter have a thickness in the order of 1 mm. For frequencies in the VHF and HF frequency bands the material thickness is in the order of the skin depth. That is why in this chapter, the CFC shells are simulated in the VHF and HF frequency bands.

This chapter is organized as follows. Section 3.2 presents the measurement results for the reflection coefficient and radiation pattern of monopole antennas mounted on metallic and CFC ground planes. Moreover, different methods of attaching an SMA connector feed to a CFC ground plane are tested. In Sections 3.3 and 3.4, monopole antennas are mounted on hollow aluminum or CFC cubic shells and operated at the frequencies of 100 MHz and 3 MHz, respectively. FEKO simulation results for the leaked electric and magnetic fields inside the shells are presented and discussed. Finally, conclusions are made in Section 3.5.

3.2 Monopole Antennas on CFC Ground Planes

Two monopole antennas using CFC and metallic ground planes were built as shown in Fig. 3.1. The ground planes are square with a side length of 15.24 cm. The

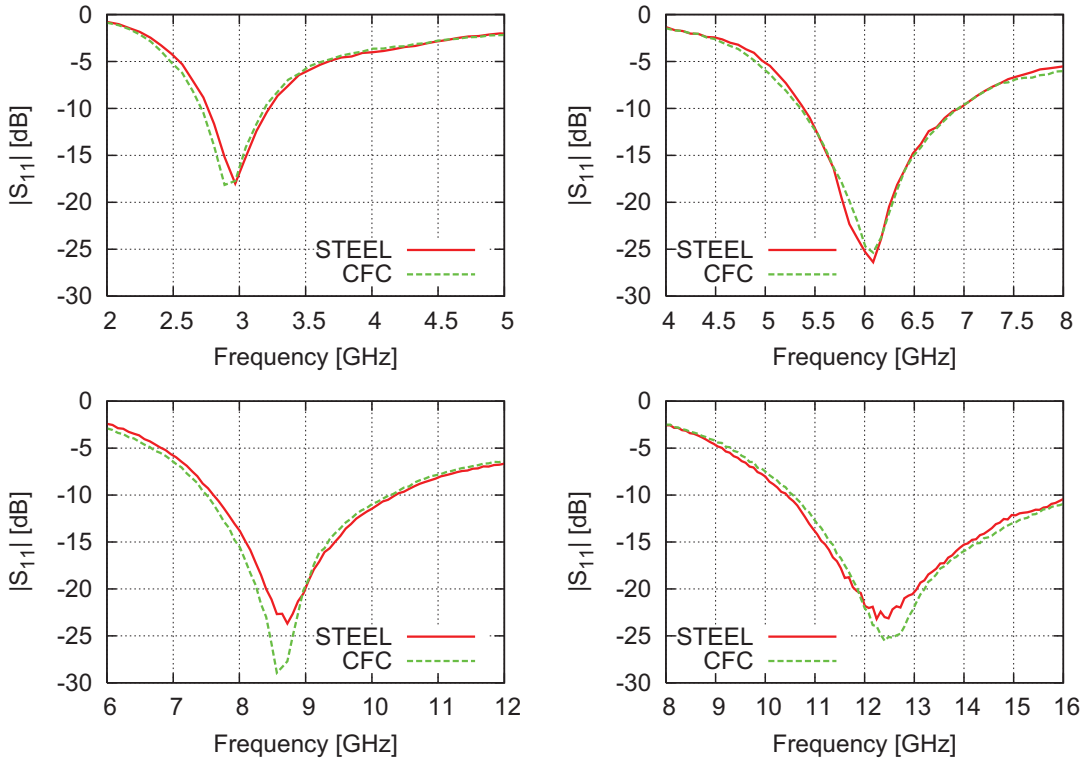

Figure 3.2: A comparison between the measured reflection coefficient of monopole antennas with CFC and steel ground planes operated at the frequencies of 3 GHz, 6 GHz, 9 GHz, and 12.5 GHz.

material of the metallic ground plane is steel with a conductivity of 5.76×10^6 S/m [4, 36]. The CFC panel is reinforced with two layers of carbon-fiber fabrics. The fiber bundles in the panel are oriented as 0/90/0/90 degrees [37]. The thickness of the CFC ground plane is 0.635 mm. The diameter of the monopole wire is 0.61 mm. During the measurement of the reflection coefficient, the lengths of the monopole antennas were adjusted for the best return loss at the frequencies of 3 GHz, 6 GHz, 9 GHz, and 12.5 GHz. The experiments are performed in order to examine effects of the metallic feed-CFC panel connection on the antenna performance. Figs. 3.2 and 3.3 compare the measured reflection coefficient and radiation pattern of the monopole antennas with CFC and steel ground planes. If we assume that the monopole wire is on the z-axis and the ground plane is on the x-y plane then the radiation pattern measurements are conducted such that the radiated E_θ in the plane of $\phi = 90°$ is

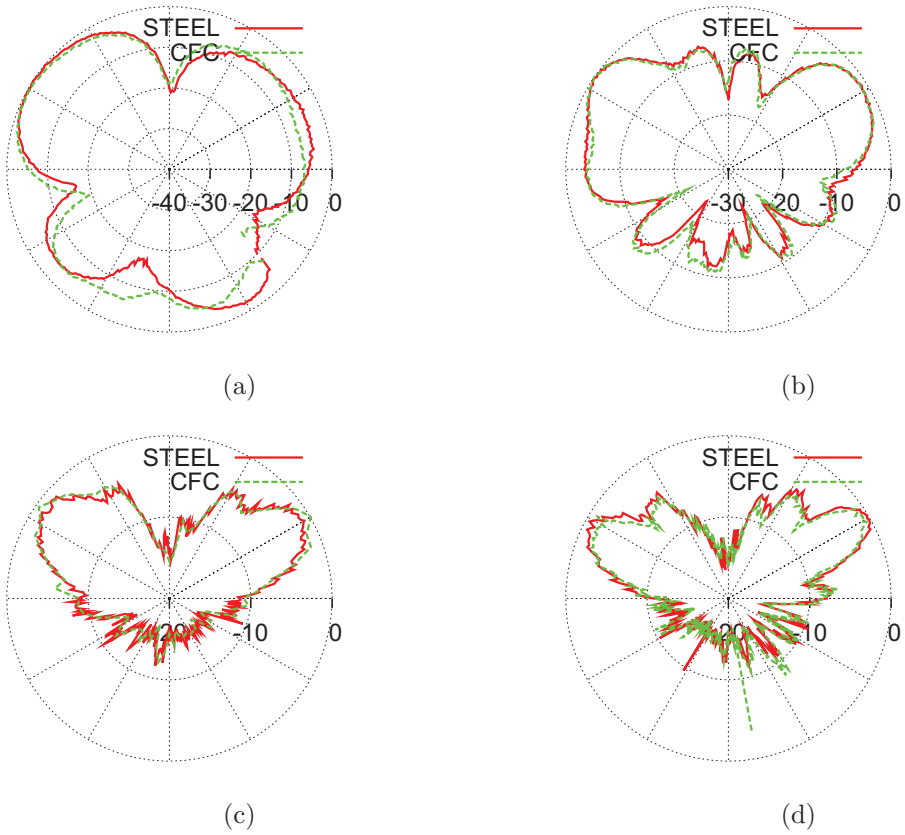

Figure 3.3: (a)-(d) are a comparison between the normalized measured radiation pattern ($|G_\theta|$) of monopole antennas with CFC and steel ground planes operated at the frequencies of 3 GHz, 6 GHz, 9 GHz, and 12.5 GHz, respectively.

measured. The radiation pattern measurements were performed at the frequencies of 3 GHz, 6 GHz, 9 GHz, and 12.5 GHz and all patterns are normalized using the same factor. It is observed that by replacing a metallic ground plane with a CFC panel the return loss and radiation pattern of the antennas are practically unchanged even at 12.5 GHz.

The establishment of the electrical contact between the SMA connector and the CFC panel is made by the two different methods which are shown in Figs. 3.4a and 3.4b. In the first method, the CFC sheet is sandpapered around the feed area so that the carbon-fibers in the panel are exposed. Then, the area is cleaned and a conductive tape is attached to the feed area. Next, the SMA connector is soldered to the conductive tape. In the second method, another copy of the same CFC panel is used.

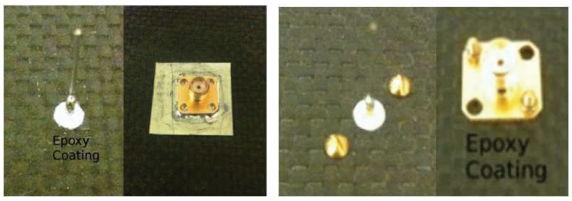

(a) (b)

Figure 3.4: Two methods of attaching an SMA connector to a CFC panel, (a) with and (b) without a patch of conducting tape.

However, no conductive tapes are employed and the feed area is not sandpapered. The SMA connector is simply attached to the CFC panel using two bolts and nuts as shown in Fig. 3.4b. The monopole antennas were operated at 3 GHz, 6 GHz, 9 GHz, and 12.5 GHz. The measured reflection coefficient of the antennas did not show dependence on the feed attachment method. In other words, both techniques provided enough coupling between the panel and SMA connector. It is believed that current flow from the SMA connector to the CFC panel can be established either through the conduction currents between the conductive tape and the carbon-fibers in the panel or through displacement currents through the capacitance that is formed by mounting the SMA feed on the CFC panel.

3.3 Interference Due to VHF Antennas

Fig. 3.5 shows a monopole antenna mounted on a hollow cubic shell. The cubic shell has a side length of $W = 3$ m and thickness of $t = 1$ mm representing part of an aircraft fuselage. Two materials for the shell are considered aluminum $\sigma_{Al} = 3.96\times10^7$ S/m [36] and CFC $\sigma = 10^4$ S/m. The monopole wire is PEC with a diameter of $D = 6$ mm and length of $l = 75$ cm. The monopole antenna is fed at the intersection of the monopole wire and top face of the shell using a "vertex port" in FEKO. In this section, the monopole antenna is operated at the VHF frequency of $f = 100$ MHz and delivered an active power of 1 W. At $f = 100$ MHz, the shell thickness equals to $2\delta_s$ and $125\delta_s$ in CFC and aluminum, respectively. The MoM solver is used to calculate

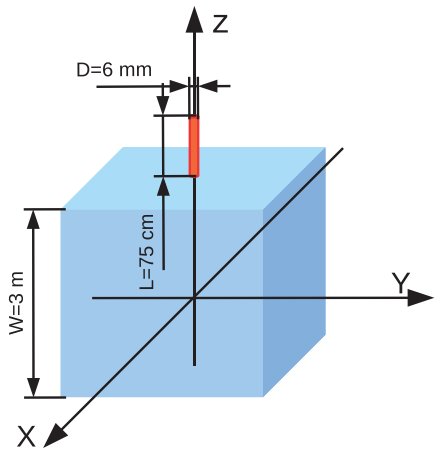

Figure 3.5: A monopole antenna mounted on a hollow cubic shell with a side length of $W = 3$ m and thickness of $t = 1$ mm. The monopole wire is PEC with a length of $l = 75$ cm and diameter of $D = 6$ mm. The material of the shell can be aluminum or CFC.

surface currents inside and outside of the shell and line currents on the wire. The magnetic symmetries with respect to the x-z, and y-z planes are imposed in order to accelerate the simulations. The monopole wire is modeled using the thin wire assumption because $D = 0.002\lambda_0 \ll \lambda_0$. Since fields inside the hollow shell are much weaker compared to fields outside the shell the surface currents inside and outside the shell are designated as unknowns by filling the shell with a dielectric material with a relative permittivity of unity [5]. The wire and the shell are meshed into 7 wire segments and 4912 triangle surface elements using the fine mesh settings in FEKO. The total number of unknowns is 3617. The electric and magnetic fields on the y-z plane inside the hollow shell are obtained and shown in Fig. 3.6. Figs. 3.6a and 3.6b reveal that there is practically no leakage of EM fields from outside into inside the aluminum shell. At the frequency of 100 MHz the thickness of the aluminum slab is $t = 1$ mm$= 125\delta_s$ where δ_s is the skin depth in aluminum. In fact, the magnitude of the leaked electric and magnetic fields are in the order of 10^{-57} V/m and 10^{-60} A/m. Furthermore, Figs. 3.6a and 3.6b could be made only on a linear scale because the fields were so weak.

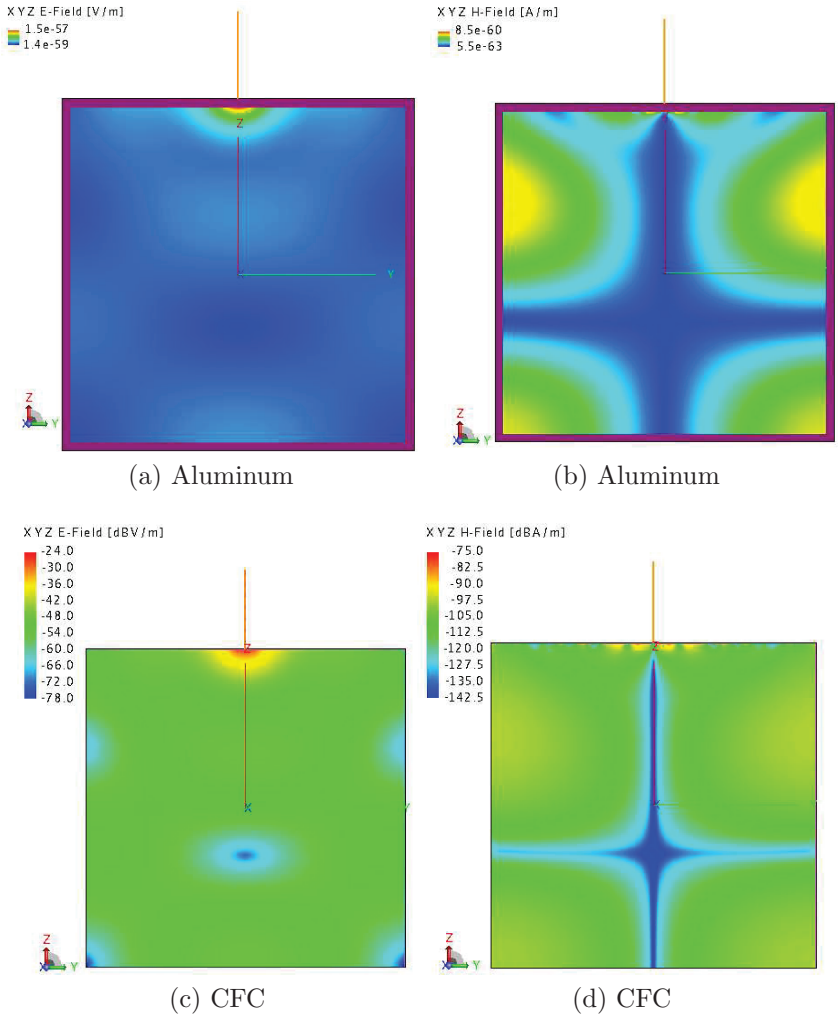

(a) Aluminum (b) Aluminum

(c) CFC (d) CFC

Figure 3.6: (a)-(d) are the electric and magnetic fields on the y-z plane inside the hollow cubic shell shown in Fig. 3.5. The average power delivered to the monopole antenna is 1 W of at the frequency of 100 MHz.

When the shell is built using CFC materials then the leakage of EM fields into the shell is shown in Figs. 3.6c and 3.6d. With reference to Figs. 3.6c and 3.6d, it is observed that electric fields are strongest (-24 dB V/m) near to the antenna feed point but decay rapidly to approximately -50 dB V/m and roughly stay the same on the y-z plane. The leaked magnetic fields are strongest (-75 dB A/m) close to the feed point but rapidly decay to approximately -110 dB A/m throughout the rest of the y-z plane. It is also observed that the magnetic fields demonstrate a local minimum on the z-axis. Therefore, field levels at one point should not be interpreted as the

field level everywhere inside the shell.

3.4 Interference Due to HF Antennas

In this section, the monopole antenna shown in Fig. 3.5 is operated at the frequency of 3 MHz. At $f = 3$ MHz, the shell thickness equals to $0.34\delta_s$ and $22\delta_s$ in CFC and aluminum, respectively. $22\delta_s$ is very thick, but $0.34\delta_s$ of the CFC shell shows potential for leakage. The geometry of the antenna is not modified and the mismatch between the monopole antenna and a 50 Ω transmission line is not of concern because FEKO is set up to automatically multiply all surface currents with an appropriate factor such that an active power of 1 W is delivered to the antenna. As a result, a comparison can be made between the leaked electric and magnetic fields into the shell at HF and VHF frequencies. At $f = 3$ MHz, we have $\lambda_0 = 100$ m. The side length of the shell is $W = 3$ m$= 0.03\lambda_0$ which is considered to be electrically small. Therefore, the mesh size is chosen based on the variations of the surface currents from one edge to other edges and not based on the wavelength. The simulations are repeated with progressively smaller mesh sizes until variations of the simulated leaked fields to the mesh size are negligible. A mesh size of $W/18 = \lambda_0/600$ is found to be small enough to represent surface currents on the shell because by choosing smaller mesh sizes the magnitude of the leaked electric and magnetic fields close to the feed point vary by a value smaller than 3 dB. The monopole wire and shell are meshed into 5 wire segments and 6232 triangle surface elements. The total number of unknowns is 4597. Figs. 3.7a and 3.7b show the magnitude of the leaked electric and magnetic fields on the y-z plane inside the aluminum shell. It is observed that the strongest electric and magnetic fields inside the shell are in the order of -210 dB V/m and -225 dB A/m near to the feed point. Figs. 3.7c and 3.7d show the magnitude of the leaked electric and magnetic fields on the y-z plane if aluminum is replaced with CFC in constructing the shell. It is observed that the strongest leaked electric and magnetic

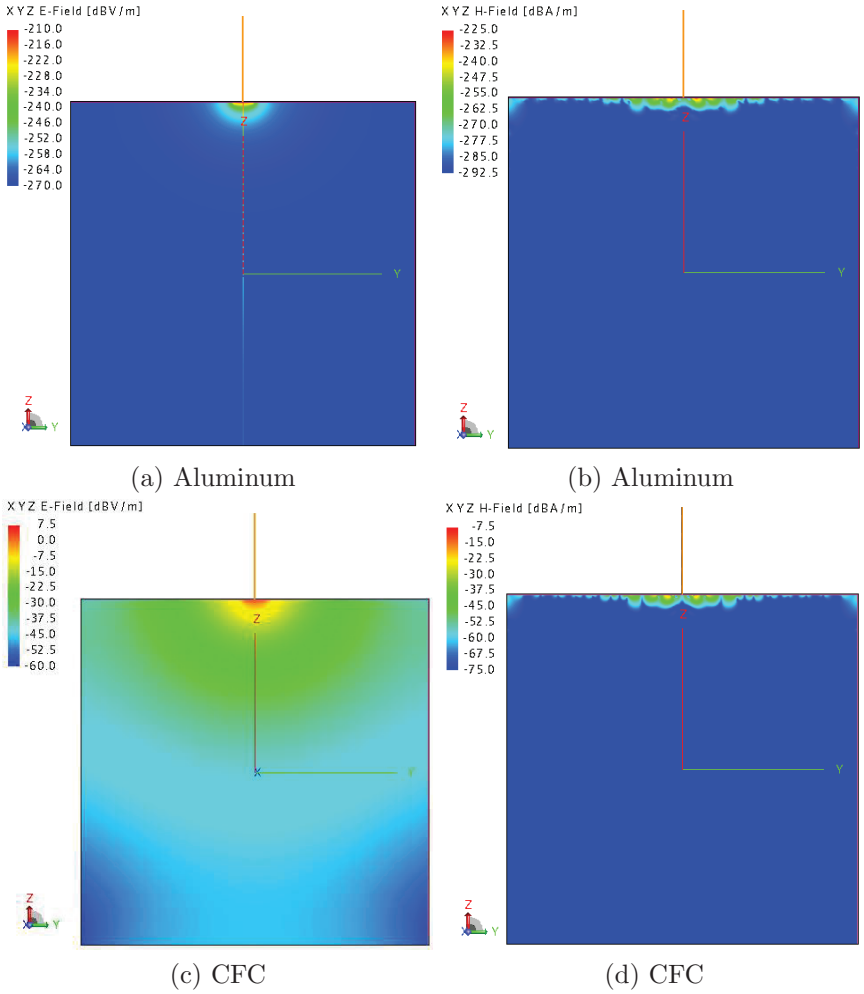

(a) Aluminum (b) Aluminum

(c) CFC (d) CFC

Figure 3.7: The electric and magnetic fields on the y-z plane inside the hollow cubic shell shown in Fig. 3.5. The average power delivered to the monopole is delivered 1 W of at the frequency of 3 MHz.

fields inside the CFC shell are in the order of 7.5 dB V/m and -7.5 dB A/m near to the feed point. Furthermore, electric and magnetic fields decay rapidly away from the feed point. Fig. 3.7 shows that by replacing metals with CFC materials variations of the electric and magnetic fields are approximately preserved but the fields strength are increased.

3.5 Conclusions

This chapter showed that by replacing a metallic ground plane with a CFC one the measured radiation pattern and feed point reflection coefficient of monopole antennas remained practically unchanged for frequencies up to 12.5 GHz. Moreover, no conductive tapes or sandpapering the feed area was found to be necessary to operate the monopole antennas on CFC ground planes. Although the antenna performance did not change by replacing a metallic ground plane with a CFC one the EMI inside CFC enclosures was much larger compared to an equivalent metallic enclosure.

Monopole antennas were mounted on hollow aluminum and CFC cubic shells and operated in the VHF and HF frequency bands. FEKO simulation results showed that by changing the enclosure's material from aluminum to CFC the field patterns inside the shell did not change but the magnitude of the leaked electric and magnetic fields were increased. In fact, the contrast between CFC and metallic shields of the same physical thickness was a source of concern at frequencies for which the barriers thickness is much larger compared to the skin depth in the metallic material but not in the CFC. It was observed that the maximum leakage of EM fields inside the shell occurred in the vicinity of the antenna feed point and could be 70 dB larger compared to other locations away from the feed area. The leakage into the shell was increased as the frequency decreased. Moreover, the quantity of the fields at one point should not be interpreted as the quantity of the fields everywhere in the shell because of the possibility of the occurrence of local nulls in the field's pattern inside the shell. When the side length of the cubic shell was much smaller than the free space wavelength the mesh size was chosen based on the variations of the surface currents on the shell and not merely based on the wavelength.

Chapter 4

Effects of Interlaminar Bondings

4.1 Introduction

The model of CFC materials which is used by Holloway *et al.* does not take into account the bonding between the reinforcing fibers in adjacent laminates [1]. However, other authors have shown that bonding between orthogonally oriented wires changes the reflection and transmission coefficients of wire meshes in free space. According to Hill and Wait, unbonded wire meshes have "superior reflecting properties" compared to the bonded wire meshes [17, 24, 25, 26]. Therefore, in this chapter the effects of bonding between the reinforcing fibers on the transmission and reflection coefficient of CFC materials are investigated. The CFC panel used in Chapter 3 was reinforced with woven fabrics. In other words, the reinforcing carbon-fibers were packed in ribbon-shaped bundles and then woven before the final CFC panel is produced. In this thesis, such a woven bundle of carbon-fibers is called a carbon-fiber fabric. The effects of bonding between orthogonally oriented carbon-fiber bundles on the reflection and transmission coefficient of CFC panels are also investigated. The electrical contact at the junction of bonded reinforcements is assumed to be ideal i.e., zero contact resistance. In this chapter, effects of embedding wire meshes with bonded and unbonded junctions in a dielectric slab on the reflection and transmission coefficients

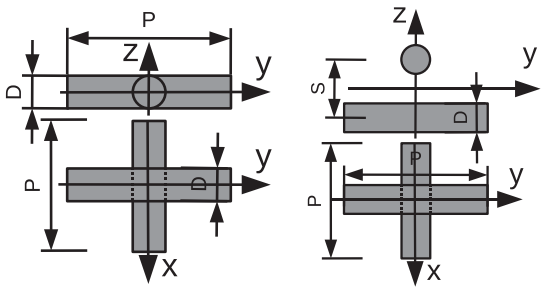

Figure 4.1: The geometry of the unit cells of bonded and unbonded PEC wire meshes in free space. D, P, and S are, respectively, the wire diameter, periodicity of the mesh, and vertical spacing between wire arrays.

are also examined.

This chapter starts with reproducing published results for the transmission coefficients of bonded and unbonded wire meshes [25]. Next in Section 4.3, effects of embedding wire meshes in a dielectric slab on the reflection and transmission coefficients are examined. In Section 4.4, the geometrical structure of CFC panels reinforced with carbon-fiber fabrics is reviewed and simplified. Then in Section 4.5, a CFC panel which is reinforced with a 1D-array of fiber bundles is simulated. Next in Section 4.6, the reflection and transmission coefficients of CFC panels reinforced by a 2D array of bonded fiber bundles are compared with those corresponding to the unbonded configuration. In this chapter, the reflection and transmission coefficients are obtained for two orthogonal polarizations. Finally, conclusions are made in Section 4.7.

4.2 Wire Meshes in Free Space

In this section, the periodic MoM solver in FEKO is used to obtain the co- and cross-polarization reflection and transmission coefficients of bonded and unbonded infinite PEC wire meshes in free space. The unit cells of the wire meshes are shown in Fig. 4.1. With reference to Fig. 4.1, D, P, and S are, respectively, the wire diameter, periodicity of the wire mesh, and spacing between the wire arrays along the z-axis.

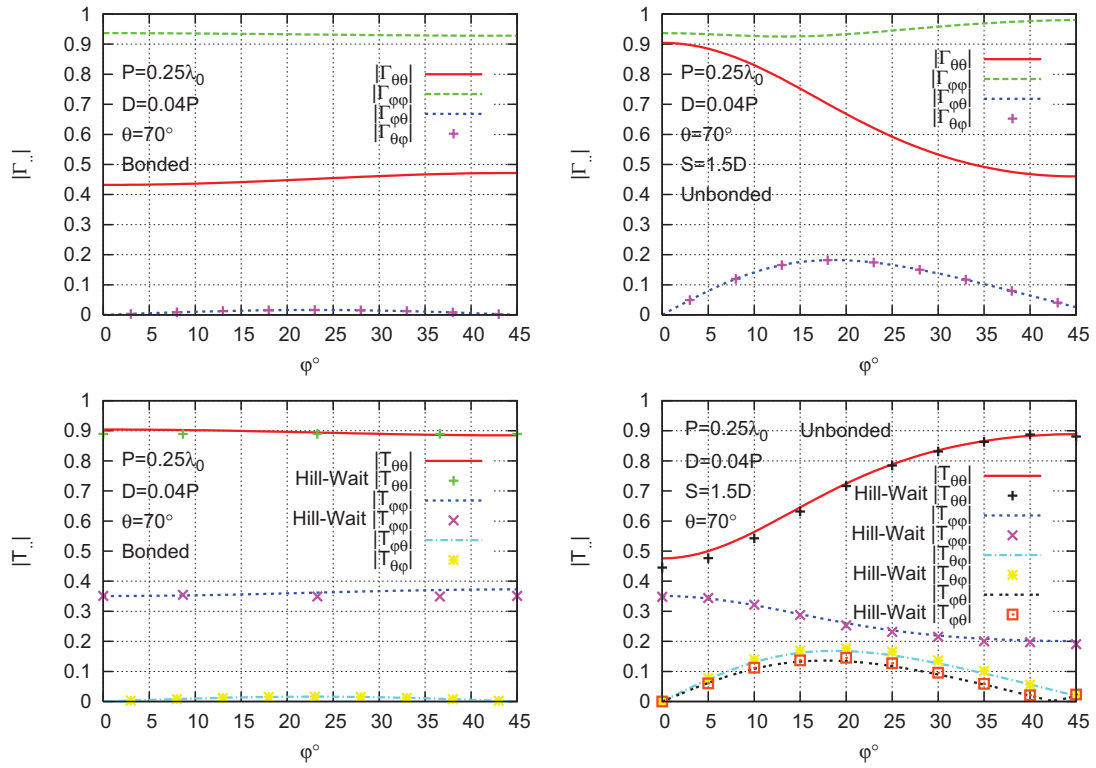

Figure 4.2: A comparison between FEKO simulation and results of Hill and Wait [3] for the co-polarization and cross-polarization transmission coefficients of bonded and unbonded PEC thin wire meshes in free space versus the azimuth angle ϕ.

The wire meshes have square unit cells because the periodicity is the same along the x- and y-axis. The wire meshes are illuminated by an incident plane wave at an oblique incident angle of $\theta = 70°$. The elevation angle θ is measured with respect to the z-axis and $\theta = 0$ denotes normal incidence. This incidence angle was chosen by Hill and Wait and the behavior of the wire meshes at other incidence angles of θ are not examined here [3]. The incident plane wave may be polarized along $\hat{\boldsymbol{\phi}}$ or $\hat{\boldsymbol{\theta}}$ in the spherical coordinate system. The $\hat{\boldsymbol{\theta}}$-polarization ($\hat{\boldsymbol{\phi}}$-polarization) is such that the incident plane wave is parallel (perpendicular) to the plane of incidence. The frequency of the incident plane wave is such that $P = \lambda_0/4$ where λ_0 is the wavelength of the incident plane wave in free space. By optionally choosing $f = 1$ GHz as the simulation frequency, the parameters in Fig. 4.1 become $D = 3$ mm, $P = 75$ mm, and $S = 4.5$ mm. The wires are analyzed using the thin wire assumption because

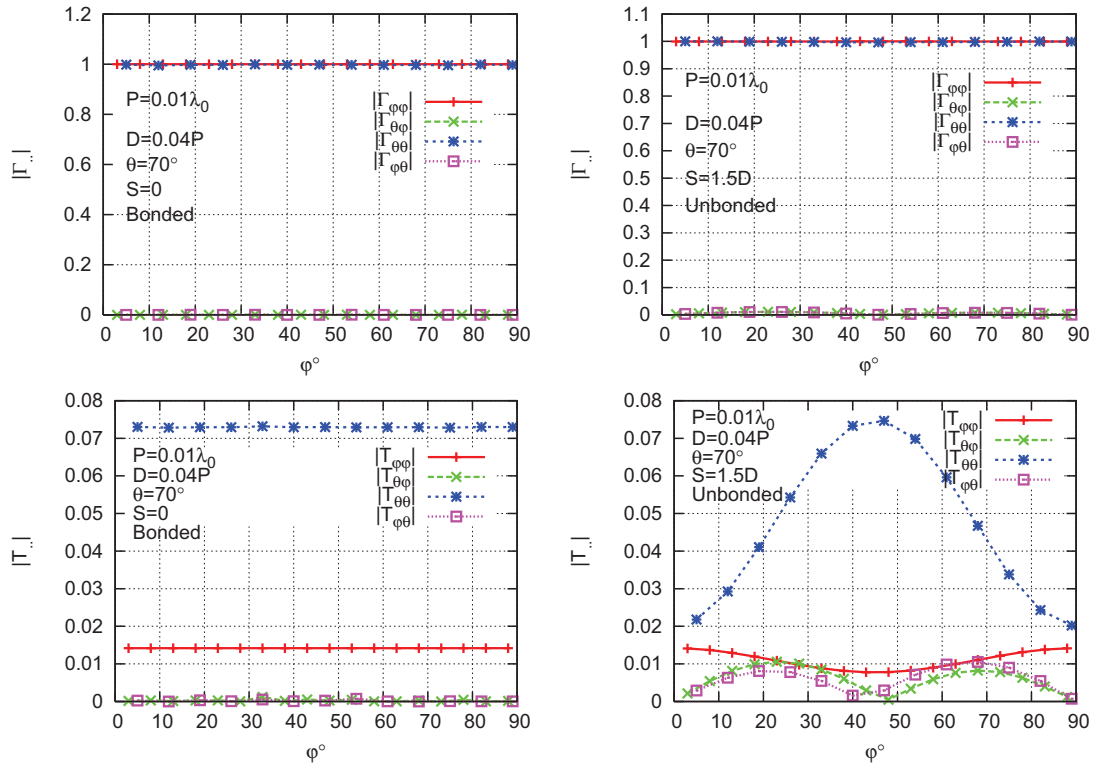

Figure 4.3: The co- and cross-polarization reflection and transmission coefficients of bonded and unbonded wire meshes in free space (Fig. 4.1) versus the azimuth angle ϕ for an oblique incident plane wave with $\theta = 70°$ at a frequency where $P = \lambda_0/100$.

$D \ll \lambda_0$. The geometries shown in Fig. 4.1 are simulated and results are presented in Fig. 4.2. With reference to Fig. 4.2, $|\Gamma_{\phi\theta}|$ denotes the magnitude of the reflection coefficient for the $\hat{\boldsymbol{\phi}}$ polarized reflected plane wave due to a $\hat{\boldsymbol{\theta}}$-polarized incident plane wave.

Hill and Wait employed a MoM solution using the Fourier expansion of the induced currents on the wires to calculate the reflection and transmission coefficients of the wire meshes. In the case of the bonded wire mesh, a discontinuity in the wire currents at the junction was also applied [17, 24, 25, 26]. Fig. 4.2 shows a good agreement between the results reported by Hill and Wait [25] and those produced by FEKO. The following conclusions are made from Fig. 4.2: 1) Bonded wire meshes may be assumed isotropic even when $P = \lambda_0/4$ because the transmission and reflection transmission coefficients are, almost, independent of the azimuth angle ϕ and the cross-polarization

components are negligible compared to the co-polarization components [25]. 2) The co-polarization transmission coefficient of an unbonded wire mesh is generally smaller than that of the bonded [17].

The reflection and transmission coefficients of bonded and unbonded wire meshes shown in Fig. 4.1 are simulated again when the frequency of the incident plane wave is reduced to $f = 40$ MHz ($P = \lambda_0/100$) while the wire mesh is not changed. The results are shown in Fig. 4.3. It is observed that the co- and cross-polarization transmission and reflection coefficients of the unbonded wire mesh for $\hat{\boldsymbol{\theta}}$- or $\hat{\boldsymbol{\phi}}$-polarized incident plane waves still show azimuth dependence despite $P \ll \lambda_0$. Moreover, for the unbonded mesh, the cross-polarization components in the transmitted and reflected waves are not negligible compared to the respective co-polarization components.

In summary, unbonded wire meshes in free space generally have a lower transmission coefficient compared to the bonded. However, unbonded wire meshes have an azimuth-dependent transmission coefficient and produce cross-polarization components.

4.3 Wire Meshes Embedded in Epoxy

The wire meshes that were discussed in the previous section are embedded in an infinite dielectric slab as shown in Fig. 4.4. The slab has a thickness of $L = 4D = 12$ mm where D is the wire diameter. The material of the dielectric slab is "epoxy resin" or simply epoxy which is widely used in manufacturing CFC materials for the aerospace industry [7]. The permittivity of epoxy resin is $\epsilon_m = 3.6\epsilon_0$ [4]. The purpose of this section is to examine effects of embedding bonded and unbonded wire meshes in an epoxy slab. With reference to Fig. 4.4, the co- and cross-polarization reflection and transmission coefficients of the embedded wire meshes are obtained for an oblique incident plane wave. The incident plane wave propagates inward and makes an angle of $\theta = 70^\circ$ with the z-axis. The incident plane wave can be polarized along $\hat{\boldsymbol{\theta}}$ or $\hat{\boldsymbol{\phi}}$ in

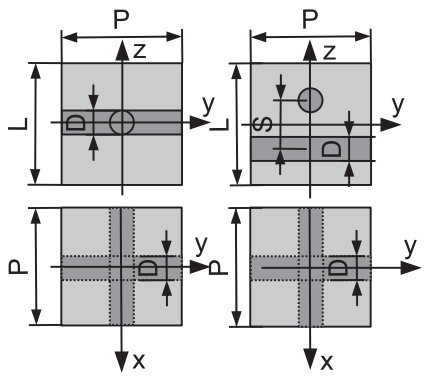

Figure 4.4: The geometry of the bonded and unbonded wire meshes embedded in an infinite dielectric epoxy slab. The thickness of the dielectric slab is $L = 4D$. D, P, and S are, respectively, the wire diameter, periodicity of the mesh, and vertical spacing between wire arrays. The wires are assumed to be PEC and the permittivity of the dielectric slab is epoxy with $\epsilon_m = 3.6\epsilon_0$ [4].

the spherical coordinate system. If the incident plane wave is polarized along $\hat{\boldsymbol{\phi}}$ then the incident electric field is parallel to the slab. The simulations are performed at $f = 40$ MHz and $f = 1$ GHz which correspond to $P = 0.01\lambda_0$ and $P = 0.25\lambda_0$ and λ_0 is the wavelength of the incident plane wave in vacuum. Therefore, the reflection and transmission properties may be identified in a wide frequency range. The embedded wire meshes shown in Fig. 4.4 are simulated using FEKO and the results are given in Fig. 4.5. With reference to Figs. 4.5(a)-4.5(d), the following conclusions at $P = 0.01\lambda_0$ are made: 1) The co-polarization reflection and transmission coefficients have variations of less than 1 dB when the azimuth angle of the incident plane wave varies from 0° to 90°. Moreover, the cross polarization components in the transmitted waves are more than 10 dB lower compared to the co-polarization components. Therefore, the embedded bonded and unbonded wire meshes may be considered isotropic. 2) For the embedded bonded and unbonded wire meshes, the transmission coefficient is approximately 17 dB larger for a $\hat{\boldsymbol{\theta}}$-polarized incident plane wave compared to a $\hat{\boldsymbol{\phi}}$-polarized one. 3) Embedding wire meshes in epoxy reduces effects of bonding between orthogonally oriented wires because the co-polarization transmission coefficients of the embedded unbonded wire mesh is less than 1 dB smaller than that of the bonded

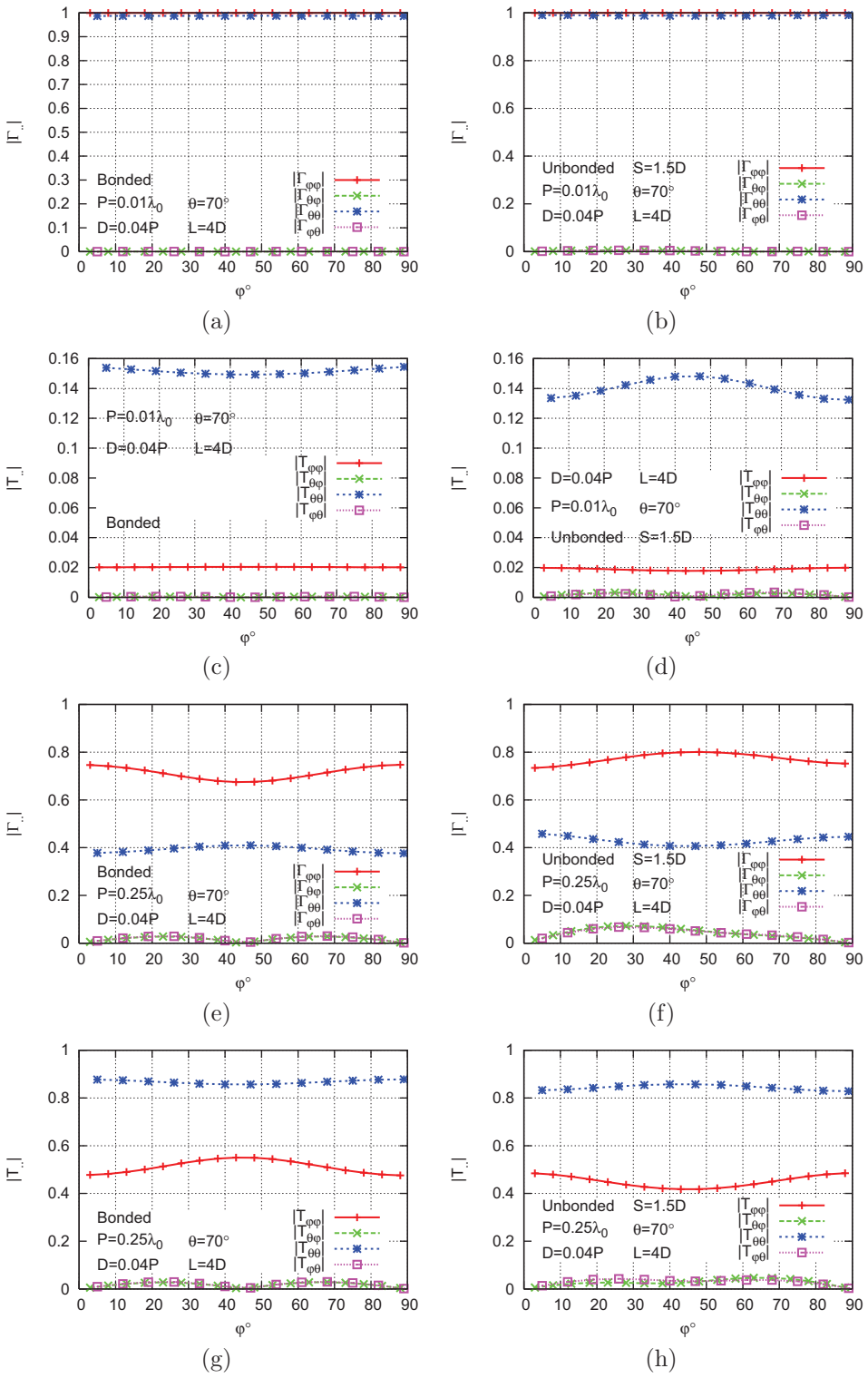

Figure 4.5: (a)-(h) are the co- and cross-polarization reflection and transmission coefficients of bonded and unbonded wire meshes embedded in an infinite epoxy slab versus the azimuth angle ϕ at an oblique incidence angle of $\theta = 70°$. Two frequencies are chosen such that $P = 0.01\lambda_0$ and $P = 0.25\lambda_0$.

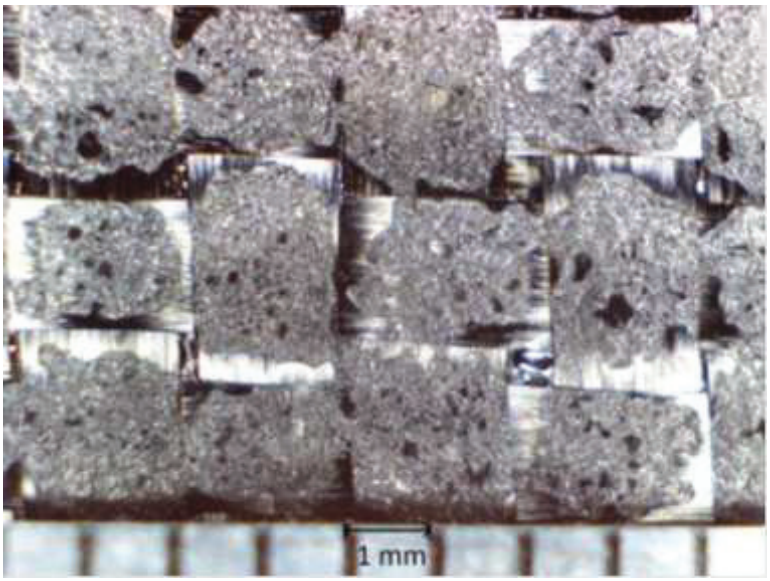

Figure 4.6: The surface of a CFC panel reinforced with two sets of carbon-fiber fabrics oriented as (0/90)/(0/90) degrees. The fabrics have a plain weave structure.

configuration.

Next, the frequency of the incident plane wave is increased to $f = 1$ GHz where $P = 0.25\lambda_0$; the simulation results are shown in Figs. 4.5(e)-4.5(h). The level of cross-polarization components and azimuth-angle dependence of the reflection and transmission coefficients are slightly increased. Moreover, it is observed that embedding bonded and unbonded wire meshes in an epoxy slab reduces the difference between the two structures. The transmission coefficient of the embedded unbonded structure is approximately 1 dB lower than that of the bonded.

In summary, embedding wire meshes in an epoxy slab made the bonding between the orthogonally oriented wires less important.

4.4 Woven Reinforcements

The surface of a CFC panel with woven reinforcements is shown in Fig. 4.6 [37]. This is the same panel that was used in Chapter 3 as antenna ground plane. The panel is composed of two layers of carbon-fiber fabrics embedded in an epoxy host

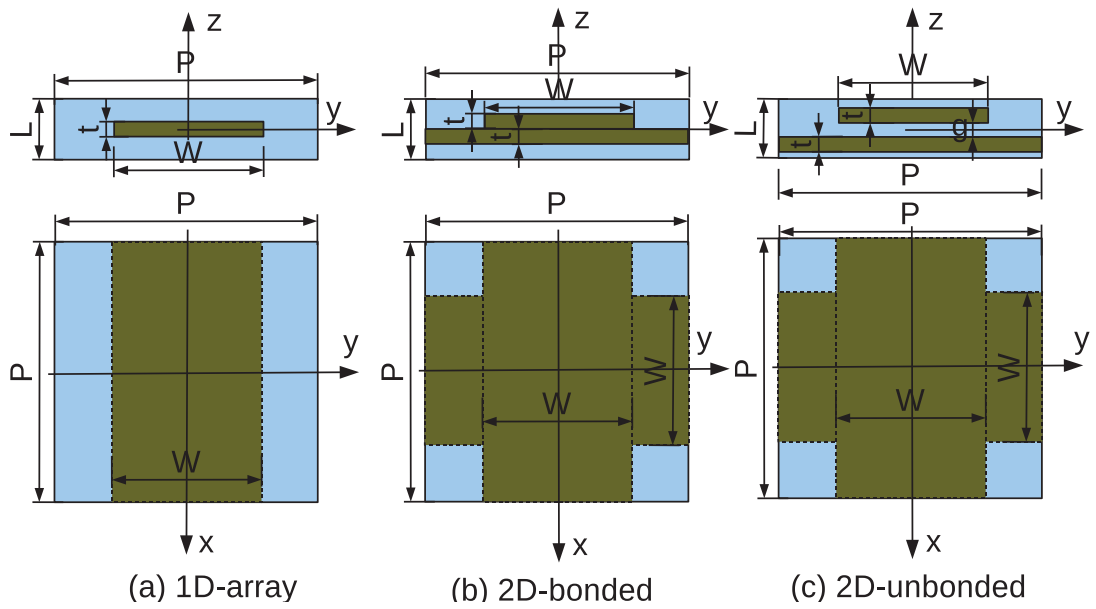

Figure 4.7: (a)-(c) are, respectively, the unit cells of a 1D, 2D-bonded, and 2D-unbonded arrays of carbon-fiber fabrics embedded in a dielectric slab. Moreover, $P = 2.2$ mm, $W = 2$ mm, $t = 0.159$ mm, and $g = 0.0159$ mm. The dielectric slab has a permittivity of $\epsilon_m = 3.6\epsilon_0$ and the carbon-fiber bundles have a conductivity of $\sigma = 10^4$ S/m.

medium [37]. The panel has a thickness of $L = 0.635$ mm. The exact geometry of a woven structure is available in [38]. For simplicity, the entanglement associated with the weaves is ignored and the cross section of the bundles is approximated to be rectangular with a width of $W = 2$ mm and thickness of $t = L/4 = 0.159$ mm. The permittivity and conductivity of the fiber bundles are assumed to be ϵ_0 and 10^4 S/m, respectively. The epoxy slab is lossless with a permittivity of $\epsilon_m = 3.6\epsilon_0$ [4]. Although the panel shown in Fig. 4.6 is reinforced with two layers of carbon-fiber fabrics the panels simulated in this chapter are reinforced with reinforcements shown in Fig. 4.7. Moreover, it is assumed that the CFC panel is infinite so that plane wave reflection and transmission coefficients may be defined. Based on the geometry shown in Fig. 4.6, the periodicity of the panel is assumed to be $P = 2.2$ mm along the x- and y-axis. Based on the physical structure of the panel, the three geometries shown in Fig. 4.7 are conceived. The panel with a 1D array of reinforcements serves as a reference panel.

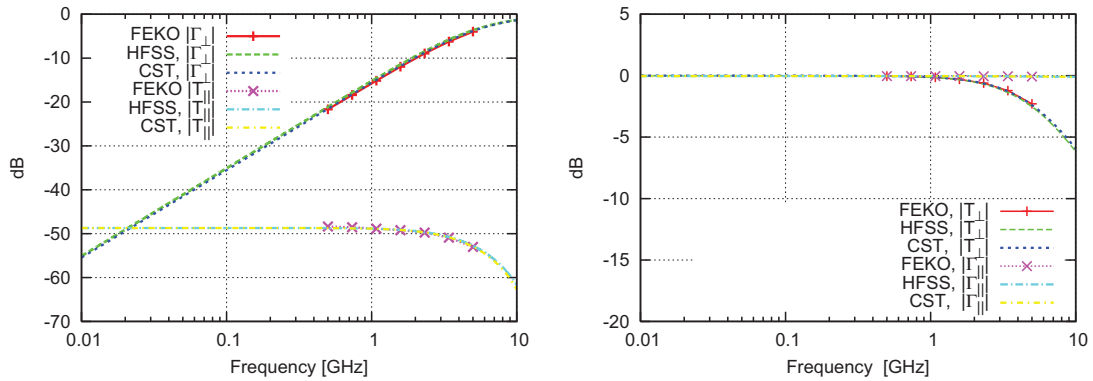

Figure 4.8: The reflection and transmission coefficients of a 1D-array of carbon-fiber fabrics embedded in a dielectric slab (Fig. 4.7a) for a normally incident plane wave. The incident plane wave may be polarized parallel (||) or perpendicular ($\perp$) to the orientation of the fiber bundles.

With reference to Fig. 4.7, the gap between the orthogonally oriented fiber bundles in the unbonded structure is denoted as g where $g = 0$ reduces the 2D-unbonded to the 2D-bonded configuration. In the following sections, the structures shown in Fig. 4.7 are simulated and the results are discussed.

4.5 1D-Array Reinforcement

Fig. 4.7a shows the unit cell of an infinite 1D-array of carbon-fiber bundles that are oriented along the x-axis with a periodicity of $P = 2.2$ mm along the y-axis. The thickness of the binding dielectric epoxy is assumed to be $L = 0.635$ mm. It is assumed that the bundles have a rectangular cross section with a width of $W = 2$ mm and thickness of $t = 0.159$ mm. The incident plane wave may be polarized parallel or orthogonal to the fabrics' orientation. Figs. 4.8a and 4.8b show the simulation results for the reflection and transmission coefficients of the embedded 1D-array for a normally incident plane wave. A good agreement between results produced by FEKO, HFSS, and CST Microwave Studio is observed [39].

Agreement between FEKO and other solvers could not be obtained for $f < 0.5$ GHz and $f > 5$ GHz. However, for $f < 0.5$ GHz a solution may be obtained

by using a larger unit cell. In the non-periodic solver metallic media in FEKO could be used for $t \leq \delta_s$ or $t \geq \delta_s$ where t is the material thickness and δ_s is the skin-depth. However, in the periodic solver the carbon-fiber bundles had to be modeled as lossy dielectric materials because $t \geq \delta_s$. But using a lossy dielectric instead of metallic medium introduces a new problem of $\lambda \ll \lambda_0$ while meshing and simulating the geometry for $f > 5$ GHz.

Figs. 4.8a and 4.8b show that at frequencies below 1 GHz, if the incident plane wave is polarized orthogonal to the bundles then the embedded 1D-array acts as a lossless dielectric slab. However, if the incident plane wave is polarized parallel to the bundles then the embedded 1D-array behaves as a lossy conducting slab. Furthermore, the transmission coefficient of the embedded 1D-array for a normally incident plane wave polarized parallel to the fibers orientation is $|T_{||}| = -49$ dB. Since $|\Gamma_{||}| \approx 0$ dB for $f \leq 1$ GHz the incident plane wave is reflected and not absorbed by the panel.

4.6 2D-Bonded and Unbonded Reinforcements

Figs. 4.7b and 4.7c show the geometries of the 2D-bonded and 2D-unbonded arrays of fiber bundles that are embedded in an epoxy slab. The gap between the orthogonally oriented fiber bundles is denoted as g. In order to examine bonding effects the gap should be chosen small compared to the bundles thickness t; Therefore, g is chosen as $t/10$. Fig. 4.9 shows the reflection and transmission coefficients of the CFC panels with 2D-bonded and 2D-unbonded reinforcements for two normally incident plane waves polarized along $\hat{\mathbf{x}}$ or $\hat{\mathbf{y}}$. The simulations are performed using FEKO, HFSS, and CST Microwave Studio and a good agreement between the solutions are obtained. Figs. 4.9a-4.9d show that at normal incidence, the transmission and reflection coefficient of the 2D-bonded structure is not dependent on the polarization of the incident plane wave for $f \leq 1$ GHz. Moreover, the transmission coefficient of

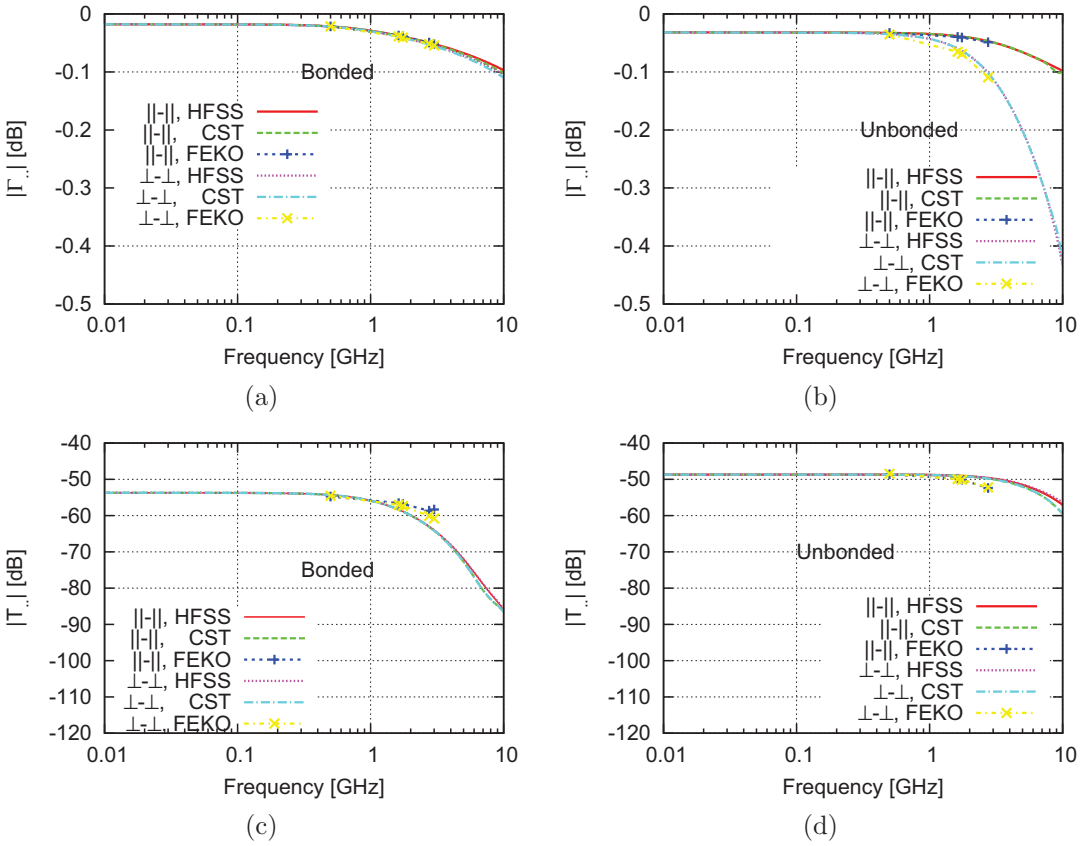

Figure 4.9: The reflection and transmission coefficients of the 2D-bonded and 2D-unbonded carbon-fiber bundles embedded in a dielectric slab, as shown in Figs. 4.7b and 4.7c. The incident plane wave propagates normal to the panels and can be polarized along the x-axis (||) or y-axis (⊥). ||-|| (⊥-⊥) represents the co-polarization component of the reflection or transmission coefficient when the incident plane wave is polarized along the x-axis (y-axis).

the 2D-unbonded configuration is -49 dB for $f \leq 1$ GHz which equals to that of the 1D-array discussed in the previous section. Fig. 4.9c shows that the transmission coefficient of the bonded structure is -54 dB for $f \leq 1$ GHz.

In summary, bonding orthogonally oriented carbon-fiber bundles causes the fiber bundles that are oriented orthogonal to the polarization of the incident plane wave to attenuate the incident plane wave also. This is an important conclusion which may be used in increasing the SE of CFC materials. At $f = 1$ GHz, the bundles thickness equals to the skin depth in the carbon-fibers. For $f \leq 1$ GHz, the bundles are completely penetrated by the incident plane wave and the SE is provided by

reflection. For $f > 1$ GHz, absorption of the incident plane wave in the carbon-fibers also contributes in SE. That is why the transmission coefficients start to decrease for $f > 1$ GHz.

4.7 Conclusions

In this chapter, effects of the bonding between orthogonally oriented wires or fiber bundles were investigated. It was assumed that structures under consideration are infinite panels so that the double periodic boundary conditions could be employed in the simulations. The wires were assumed to be PEC and were modeled using the thin wire approximation. For wire meshes in free space, FEKO simulation results for the co- and cross-polarization transmission coefficients were validated with published results. It was observed that unbonded wire meshes in free space were preferable over the bonded wire meshes from a SE point of view. However, embedding the wire meshes in an epoxy slab reduced the effects of bonding on the transmission and reflection coefficients. In other words, although unbonded wire meshes in free space are preferable over bonded wire meshes from a SE point of view, that advantage is weakened by embedding unbonded wire meshes in a dielectric material. The reflection and transmission coefficients of CFC panels with reinforcements in the form of fiber bundles were obtained. It was assumed that the reinforcing fiber bundles had a rectangular cross section with a width of 2 mm and thickness of 0.159 mm. The fiber bundles were modeled using lossy dielectric materials with a conductivity of 10^4 S/m. Simulation results showed that bonded fiber bundles were preferable over the unbonded from a SE point of view. In fact, the bondings caused the bundles that are oriented orthogonal to the polarization of the incident plane to contribute in the shielding process. This is a useful point which may be employed to enhance the shielding capabilities of CFC panels.

Chapter 5

Shielding Effectiveness of CFC Enclosures

5.1 Introduction

CFC materials can be modeled as isotropic lossy conducting media with a conductivity in the order of $\sigma = 10^4$ S/m [15]. In this chapter, the capabilities and limitations of FEKO in modeling conducting materials are investigated. The focus is on the Surface Integral Equations (SIE) solutions to SE problems involving CFC materials. By default, FEKO treats conducting materials as impedance sheets rather than generally penetrable objects because fields decay very rapidly inside conducting materials [32]. FEKO User's manual recommends Modeling conducting materials using "Metallic Media" [32]. "Metallic Media" that are bound by free space regions are modeled as impedance sheets [32]. The sheet impedance Z_s is the proportionality constant between the tangential electric field and the electric surface currents on the sheet [32]. The value of the sheet impedance is automatically calculated by FEKO. If the sheet impedance has been obtained through measurement techniques or other analytical solutions then the user can also use custom values for the sheet impedance. In order to validate FEKO's ability in calculating large SE quantities inside CFC

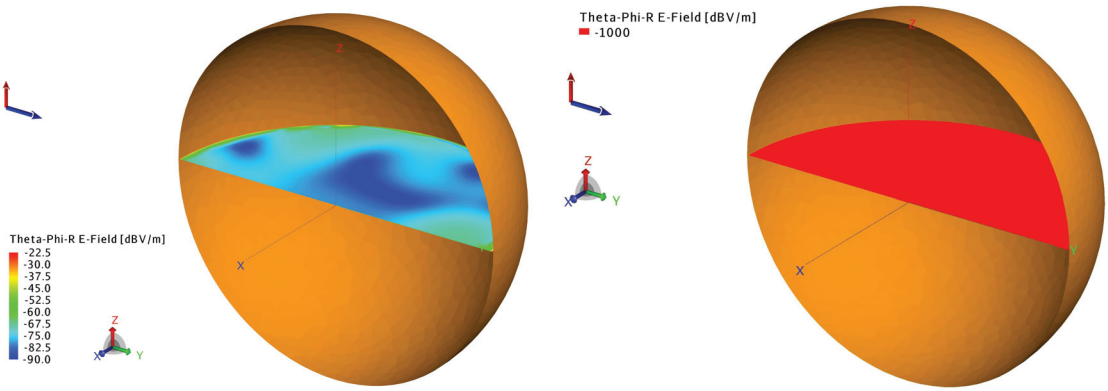

(a) (b)

Figure 5.1: (a) and (b) are the FEKO Simulation results for the total electric field inside a hollow spherical PEC shell with a radius of 3 m for an incident plane wave given by $\mathbf{E} = \hat{\mathbf{z}}e^{-jk_0 y}$ at the frequency of 100 MHz. In case (a) fields inside the shell are obtained using the free space MoM whereas in case (b) fields are obtained by using the inside-outside formulation [5].

enclosures certain benchmark solutions are generated in this chapter.

This chapter is outlined as follows. In Section 5.2, the inside-outside formulation is elaborated and its difference with the free space MoM is explained. An infinite CFC panel modeled as a lossy dielectric material is simulated in FEKO and the results are compared with the analytic solution in Section 5.3. In Section 5.4, benchmark numerical results for the electric and magnetic SE inside a hollow spherical CFC shell are presented and compared with FEKO simulation results. Finally, conclusions are made in Section 5.5.

5.2 The Inside-Outside SIE Formulation

If a closed PEC surface is bound by free space regions then FEKO uses the free space MoM to find the electric surface currents on the PEC surface such that the scattered and incident electric fields cancel each other everywhere inside the PEC shell. This requires perfect cancellation of the tangential components of the incident and scattered electric fields everywhere on the PEC surface. In fact, a very small

error in the cancellation of the tangential electric fields causes large SE errors on the dB-scale [5].

Fig. 5.1a shows the cross sectional view of a hollow spherical PEC shell with a radius of 3 m which is illuminated by a plane wave with a frequency of 100 MHz. The shell is bound by free space regions in the FEKO model and the free space MoM is used to solve the problem by default. Using the standard mesh settings, the electric fields inside the shell on the x-y plane are obtained and results are shown in Fig. 5.1a. The magnitude of the electric fields inside the shell should be 0 V/m or $-\infty$ dB V/m. Effects of the imperfect cancellation of the incident and scattered fields are evident in Fig. 5.1a. It is observed that the electric fields produced by the surface currents on shell are capable of canceling the incident electric field down to a range of -22.5 dB V/m to -90 dB V/m. Fig. 5.1a also shows that the error tends to be larger in the vicinity of the walls of the shell.

If the SIE is formulated such that total fields inside the shell are given by one set of electric surface currents and the scattered fields outside the shell are obtained by another set of surface currents then the inside-outside formulation is obtained [5]. Obviously, the inside-outside formulation is based on the surface equivalence principle (SEP) [40]. Using the inside-outside formulation, perfect cancellation of the incident and scattered fields inside the PEC shell is no longer required and large SE quantities can be obtained. In order to replace the free space MoM with the inside-outside formulation the only requirement is to change the material inside the hollow PEC shell from free space to a dielectric material with a relative permittivity of unity [5]. Having done that, the electric fields inside the shell are shown in Fig. 5.1b. It is observed that the magnitude of the electric fields inside shell is now as low as -1000 dB V/m. In fact, 0.0 on a linear scale is shown as -1000 dB on a dB-scale in FEKO. The magnitude of the magnetic fields inside the shell is not shown for the sake of brevity but they are also -1000 dB A/m on the x-y plane inside the shell. Application of the inside-outside SIE formulation requires twice as many unknowns as the free space

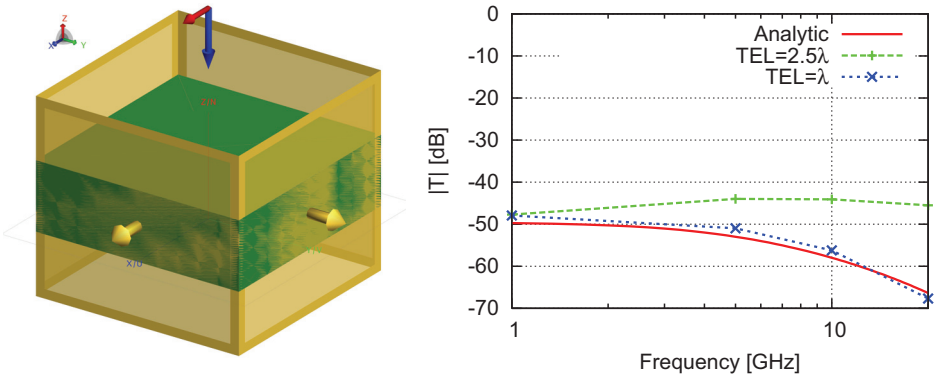

(a) (b)

Figure 5.2: (a) The geometry of the unit cell of an infinite CFC panel modeled as a dielectric material with $\sigma = 10^4$ S/m. The panel thickness is 0.159 mm. The triangle edge length (TEL) denotes the mesh size in FEKO. TEL is expressed in terms of the wavelength in the CFC panel. (b) The transmission coefficient of the panel shown in Fig. 5.2a for a normally incident plane wave. The incident plane wave is polarized along the x-axis and its frequency varies from 1 GHz to 20 GHz.

MoM. In return, it makes it possible to calculate very large SE quantities. In Section 5.4, capabilities of the inside-outside formulation will be further explored. The SE of the simplest closed CFC structure which is an infinite CFC slab is calculated in the next section.

5.3 SE of an Infinite CFC Panel

In order to obtain the SE of an infinite CFC panel whose thickness is larger than the skin-depth in the material a solution could only be obtained if the panel were modeled as a lossy dielectric material with $\sigma = 10^4$ S/m. The geometry of the problem is shown in Fig. 5.2. The panel has a thickness of $t = 0.159$ mm and the double periodic boundary conditions are used in the simulations.

The transmission coefficient of the panel for a normally incident plane wave is calculated in the frequency range of 1 GHz to 20 GHz. The skin depth in the panel is $\delta_s = 0.159$ mm and $\delta_s = 0.036$ mm at $f = 1$ GHz and $f = 20$ GHz, respectively. The width of the unit cell in Fig. 5.2 is chosen as $W = 5\lambda$ where λ is the wavelength in

the panel at the frequency of the incident plane wave. Inside the CFC panel and at $f = 1$ GHz, $\lambda = 1$ mm but $\lambda_0 = 300$ mm; consequently, we have $W = 5\lambda = \lambda_0/6 = 5$ mm. Although in the FEKO examples guide a unit cell size of $\lambda_0/2$ was employed a choice of $W = \lambda_0/6$ had to be made because the periodic solver crashed for $W > \lambda_0/6$ [41].

The simulation results for the transmission coefficient of the panel are compared with the analytic solution in Fig. 5.2b. The simulations are performed with two different mesh sizes i.e., triangle edge length (TEL)=2.5λ and TEL=λ. Fig. 5.2b shows that satisfactory results are obtained only for TEL=λ. It should be noted that at normal incidence the surface currents are constant with no variations on the surface. In other words, Fig. 5.2b shows that in SE calculations the mesh size on the surface of a dielectric material should be chosen smaller than or equal to the material wavelength.

The SIE formulation associated with Poggio, Miller, Chang, Harrington, Wu and Tsai (PMCHWT) is used by FEKO to model dielectric materials. In other words, FEKO uses the PMCHWT formulation to calculate the surface currents on the top and bottom faces of the unit cell. In the PMCHWT formulation, the SEP is employed to postulate the existence of equivalent electric and magnetic surface currents on the boundary of the scatterer such that $\mathbf{J_s}$ and $\mathbf{M_s}$ produce the scattered fields outside the scatterer but the total fields inside the obstacle. $\mathbf{J_s}$ and $\mathbf{M_s}$ are found by imposing boundary conditions associated with the continuity of the tangential electric and magnetic fields on the boundary of the scatterer. The elements of the MoM matrix in the PMCHWT formulation are dependent on the wavelength in the conducting material as well as the free space wavelength [42, 43]. For materials with a conductivity in the order of 10^4 S/m, this leads to an excessive simulation time and loss of accuracy in SE problems. Therefore, instead of using the exact formulation alternative SIE formulations along with approximate boundary conditions are widely used when modeling conducting media.

Therefore, modeling CFC panels as lossy dielectric materials in SE calculations requires extensive simulation resources and is not efficient. In order to eliminate the dependence of the mesh size to the material wavelength the inside-outside formulation is employed in FEKO [5].

5.4 SE Inside a Hollow CFC Shell

In this section, it is assumed that a hollow spherical CFC shell in free space is illuminated by a plane wave of $\mathbf{E}^i = \hat{\mathbf{x}}e^{-jk_0z}$ where $k_0 = 2\pi f\sqrt{\mu_0\epsilon_0}$ and f varies in the range of 1 MHz to 100 MHz. The shell has a radius of 3 m, thickness of 1 mm, and conductivity of $\sigma = 10^4$ S/m. The shell's center is coincident with the origin of the coordinate system. In this section, we are interested in calculating the electric and magnetic fields inside the shell.

The problem of scattering by concentric spheres is considered in [44]. Calculating the analytic solution for the SE inside a hollow spherical shell is straightforward [45]. However, if the shell is a made of a conducting material with $\sigma = 10^4$ S/m then the analytic solutions could not be numerically evaluated because of an overflow in the involving Schelkunoff Bessel functions. A method is developed to eliminate this problem and is presented in Appendix A.

The procedure for defining the problem in FEKO is as follows. At first, a metallic medium named "cfc" with a conductivity of 10^4 S/m is defined. Next, a dielectric medium named "air" with a relative permittivity of unity is created. Then, a solid sphere with a radius of 3 m is constructed in FEKO and the material of the sphere is changed from the default PEC to "air". Finally, the surface ("face") of the sphere is set to be "cfc" with a thickness of 1 mm. Fig. 5.3 shows the FEKO simulation results and the analytic solutions for the electric fields $|\mathbf{E}(x = 0, y = 0, z = 0)|$ and normalized magnetic fields $|\eta_0\mathbf{H}(x = 0, y = 0, z = 0)|$ at the shell's center; η_0 is the characteristic impedance of the free space. The SE to electric or magnetic fields at

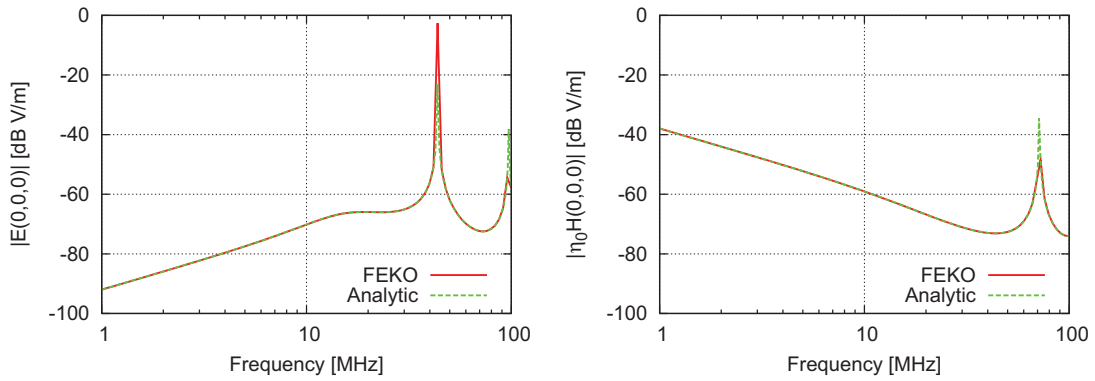

Figure 5.3: The analytic and simulation results for the electric and normalized magnetic fields at the center of a hollow spherical CFC shell with a radius of 3 m, thickness of 1 mm, and conductivity of $\sigma = 10^4$ S/m. The incident plane wave is $\mathbf{E}^i = \hat{\mathbf{x}}e^{-jk_0 z}$.

shell's center would be the negative of the values that are read from Fig. 5.3. A good agreement between the FEKO and analytic solution is observed in the frequency span of 1 MHz to 100 MHz. For a hollow spherical shell with a radius of 3 m, the $TM^r_{m,1,1}$ and $TE^r_{m,1,1}$ modes have the resonance frequencies of $f = 43.672$ MHz and $f = 71.508$ MHz, respectively [45]. Fig. 5.3 shows that at the dominant resonance frequency of the cavity, the leakage of the electric fields into the cavity is increased by almost 60 dB.

At frequencies below the dominant mode of the cavity ($TM^r_{m,1,1}$), the electric and magnetic fields at the shell's center behave differently. In fact, as the frequency decreases, the magnitude of the leaked electric fields reduce by 20 dB/decade while the magnitude of the leaked magnetic fields increase by 20 dB/decade. Therefore, the leaked magnetic fields as well as electric fields inside the shell must be examined to ensure EMC requirements are met. In Appendix A, it is shown that at the center of the shell, the analytic solution for the magnitude of the electric and magnetic fields reduces from a summation of infinite terms to only one term.

The sharp increase in leakage of the fields at the cavity's resonance frequencies are further examined by calculating the electric and magnetic fields inside the shell on the z-axis and at the frequencies of $f = 43.672$ MHz and $f = 71.508$ MHz corresponding

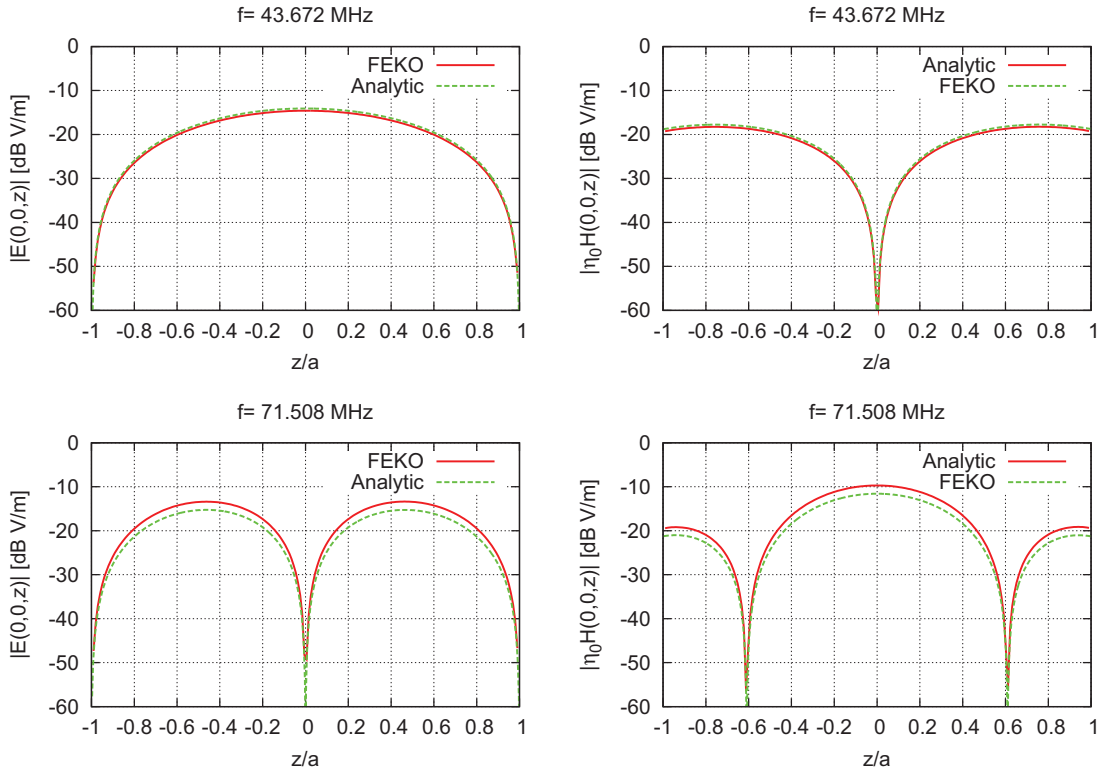

Figure 5.4: The analytic and simulation results for the electric and magnetic fields on the z-axis inside a hollow spherical CFC shell with a radius of 3 m, thickness of 1 mm, and conductivity of $\sigma = 10^4$ S/m. The incident plane wave is $\mathbf{E}^i = \hat{\mathbf{x}}e^{-jk_0z}$ where k_0 is wavenumber of the incident plane wave at the frequencies of 43.672 MHz and 71.508 MHz.

to the $TM^r_{m,1,1}$ and $TE^r_{m,1,1}$ resonances of the spherical cavity. Fig. 5.4 shows a very good agreement between the FEKO simulation results and analytic solutions for the electric and magnetic fields on the z-axis. In order to obtain the agreement, the mesh size is chosen as TEL=$\lambda_0/20$ where λ_0 is the wavelength of the incident plane wave in free space. The SE of an infinite CFC panel with a thickness of 1 mm to a normally incident plane wave at $f = 43.672$ MHz is 66 dB. However, the electric SE of the same CFC material when used as a hollow spherical shell can be as low as 15 dB at cavity resonances. Fig. 5.4 shows that the magnetic SE inside the shell can be as low as 10 dB at cavity resonances.

5.5 Conclusions

This chapter was focused on the calculation of the electric and magnetic SE inside CFC enclosures. It was observed that an approximate solution based on using metallic media in FEKO should replace the exact PMCHWT formulation when modeling penetrable materials with $\sigma = 10^4$ S/m. This was proved by showing that the if a CFC panel is modeled as a lossy dielectric material then the mesh size has to be chosen as small as the wavelength in the CFC material. Using the problem of scattering by a hollow spherical PEC shell, the free space MoM and inside-outside formulations were compared. In the free space MoM formulation the sum of the surface currents on the inner and outer sides of the PEC shell was calculated and the fields everywhere in space were the summation of the incident and scattered fields. Using this formulation the maximum SE that could be calculated near to the walls of a shell was limited to 22.5 dB. This is because the cancellation of the incident and scattered fields could not be perfect because of discretization of the surface currents and finite precision arithmetic operations. It was shown that the inside-outside formulation is capable of calculating SE quantities as large as 1000 dB at the expense of doubling the number of unknowns. In the inside-outside formulation, the electric surface currents inside and outside the shell were individually calculated. In order to replace the free space MoM with the inside-outside formulation in FEKO the CFC panel should be backed by a dielectric material with a permittivity of ϵ_0.

For the SE inside a hollow spherical CFC shell, FEKO simulation results were compared with the analytic solution and a good agreement was obtained. To calculate SE quantities inside the shell the mesh size was chosen as $\lambda_0/20$ which is smaller than the default value of $\lambda_0/12$. It was observed that the SE was significantly compromised at the cavity's resonance frequencies. At frequencies much smaller than the dominant resonance of the cavity, as the frequency was decreasing, the electric SE increased by 20 dB/decade while the magnetic SE decreased by 20 dB/decade. While evaluating the benchmark analytic solutions for the SE inside a hollow spherical CFC shell

certain numerical difficulties were encountered and resolved.

Chapter 6

Conclusions and Future Work

6.1 Conclusions

A literature survey in Chapter 1 showed that CFC materials could be modeled as conducting materials with a conductivity in the order of 10^4 S/m. Furthermore, the radiation pattern and gain of antennas that were mounted on metallic ground planes were practically unchanged by replacing the ground plane with a CFC one. Therefore, the focus of the thesis was on the calculation of the SE of CFC structures using FEKO.

In Chapter 2, the reflection and transmission coefficients of the idealized model of CFC panels with one, two, and four laminates were obtained with the FEKO skin-effect approximation and the results were validated with published literature and other commercially available software. Using homogenization techniques the inhomogeneous structure of the idealized model of CFC panels were simplified to an equivalent multilayer structure. All layers of the equivalent multilayer model were homogeneous but certain layers were anisotropic. The tensor conductivity and permittivity of each layer of the equivalent multilayer model were specified in FEKO. A stack-to-sheet conversion approach was used to shrink the equivalent multilayer model to an impedance sheet with zero thickness. Using the skin-effect approximation the

total VEP currents that penetrated a CFC panel were reproduced on an impedance sheet. Furthermore, the VEP currents normal to a CFC panel were ignored. The tensor sheet impedance of a CFC panel was found such that the tangential electric field in the panel equaled to that on the impedance sheet. Therefore, the CFC panel had to be thin with respect to the material wavelength so that the electric field was almost constant in the panel. It was observed that approximations made in the skin-effect model could be ignored in simulation results for the reflection coefficient. However, simulation results for the transmission coefficient were in agreement with exact solutions only if the panel was thin with respect to the material wavelength. It was shown that the stack-to-sheet conversion and not the homogenization techniques limited the largest frequency at which the FEKO skin-effect approximation could be used in SE calculations. Furthermore, to use the skin-effect approximation the panel's physical thickness had to be thin compared to the panel's lateral dimensions. The magnetic SE at the center of a hollow cubic shell with a CFC face was calculated using the skin-effect and inside-outside approaches and the results were compared with published literature. Although results of the skin-effect model were in agreement with other solutions when the panel's thickness was smaller than or equal to the skin-depth, application of the skin-effect approximation in SE calculations required a very fine mesh. That said, for a fixed mesh size, the skin-effect model created as many unknowns as if the CFC panel composed of multiple laminates was simply a PEC sheet. This was the greatest merit of the skin-effect approximation which made it useful for calculating the far-zone scattered fields of electrically large CFC structures, such as aircraft. In fact, if a CFC panel is not quasi-isotropic or its thickness is not larger than the skin depth in the panel then it must be modeled as a laminated material using the skin-effect approximation rather than a PEC sheet.

In Chapter 3, it was shown that the reflection coefficient and radiation pattern of monopole antennas operated up to a frequency of 12.5 GHz were not altered if the metallic ground plane was replaced by a much lighter CFC one. Sandpapering

the feed area or using conductive tapes were found to be unnecessary for operating monopole antennas mounted on CFC ground planes.

Monopole antennas mounted on metallic and CFC cubic shells were operated at the frequency of 3 MHz and 100 MHz and the radiated EMI inside the shells were calculated. It was shown that by replacing aluminum with CFC the pattern of the leaked fields did not change but the strength of the leaked fields increased. It was observed that as the frequency decreased effects of the lower conductivity of CFC panels compared to the metallic ones became more of concern because a CFC barrier with the same physical thickness as the metallic panel might no longer be much thicker than the skin-depth in the barrier. The maximum leakage of EM fields inside a cubic CFC enclosure occurred near to the feed point and could be 70 dB larger compared to other locations in the shell away from the feed point. The leakage of EM fields into the shell increased as the frequency decreased. Furthermore, the quantity of fields at one point could not be interpreted as the general value of fields in CFC enclosures.

In Chapter 4, effects of bonding between orthogonally oriented reinforcements were examined. PEC wire meshes were modeled using the thin wire assumption and reinforcements in the form of carbon-fiber bundles had to be modeled as dielectric materials with $\sigma = 10^4$ S/m. The published results for the co- and cross-polarization transmission coefficients of bonded and unbonded wire meshes were reproduced using the periodic MoM solver in FEKO. It was observed that in free space, wire meshes with unbonded junctions were preferable to wire meshes with bonded junctions from a SE standpoint. However, bonded wire meshes were more isotropic compared to the unbonded and created weaker cross-polarization components. It was shown that embedding wire meshes in an epoxy slab weakened effects of the bonding at the junctions.

Based on the geometry of a purchased CFC panel, reinforcements in the form of carbon-fiber bundles were conceived. The carbon-fiber bundles had a width of 2 mm and thickness of 0.159 mm. It was shown that bonding the junctions improved the SE

of CFC panels with reinforcements in the form of carbon-fiber bundles. Furthermore, in the case of unbonded junctions the reinforcements that were oriented orthogonal to the orientation of the polarization of the incident plane wave were transparent to a normally incident plane wave. Moreover, the periodic solver in FEKO took much longer simulation time compared to HFSS or CST Microwave Studio for the same problem involving carbon-fiber bundles.

Chapter 5 was focused on EM modeling of conducting materials with $\sigma = 10^4$ S/m in SE calculations. To calculate the SE of an infinite CFC panel at a frequency for which the panel's thickness was larger than the skin-depth the panel had to be modeled as a dielectric material with $\sigma = 10^4$ S/m. It was observed that the exact PMCHWT formulation which was used for modeling dielectric materials required that the mesh size be determined by the wavelength in the CFC material and not free space. Therefore, approximate instead of exact formulations were adapted for calculating the SE of conducting structures.

The maximum dB-quantity of the SE that could be obtained using the free space MoM was found to be very sensitive to the numerical errors associated with the cancellation of the incident and scattered fields. Furthermore, the free space MoM was based on calculating the sum of the surface currents on both sides of sheets while the inside-outside formulation calculated currents on each side of sheets. That was the reason that the inside-outside formulation created twice as many unknowns as the free space MoM did. The total fields inside a hollow spherical PEC shell illuminated by a plane wave were calculated using the free space MoM and inside-outside formulations. When the free space MoM was employed, the electric fields inside the shell were in the order of -22.5 dB V/m near to the walls of the shell while in the inside-outside formulation the electric fields were in the order of -1000 dB V/m.

The SE quantities obtained using the inside-outside formulation were validated by creating benchmark solutions for the SE inside a hollow spherical CFC shell. The analytic solution needed to be modified to overcome the overflow of the Schelkunoff

Bessel functions that were associated with the conducting media. In order to obtain agreement with the benchmark solutions FEKO simulations were performed using the inside-outside formulation and a mesh size of $\lambda_0/20$ instead of the default value of $\lambda_0/12$. At frequencies below the resonance of the dominant mode of the spherical cavity the SE to electric fields increased by 20 dB/decade as the frequency decreased but the magnetic SE was decreasing with the same rate. The SE could be reduced by 60 dB at the resonance frequencies of the spherical cavity.

6.2 Future Work

In future work, the periodic MoM solver in FEKO should be accelerated because at this time the FEKO's periodic solver often requires a much longer simulation time compared to other commercially available FEM or finite integration technique (FIT) solvers.

The CFC panel reinforced with carbon-fiber bundles was simulated up to 10 GHz. It would be advantageous to simulate the panel at higher frequencies and verify the simulation results and the differences between the bonded and unbonded configurations. Moreover, effects of a non-zero contact resistance at the junctions of bonded and unbonded reinforcements on the SE can also be investigated.

Materials with $\sigma = 10^4$ S/m cannot always be treated using the inside-outside formulation e.g., a periodic array of carbon-fiber bundles. In fact, it is necessary to modify the MoM solver so that it can efficiently handle materials with $\sigma = 10^4$ S/m in SE calculations using an exact SIE formulation.

The inside-outside formulation in FEKO could not be applied to anisotropic layered media. This is another feature that can be added to FEKO.

It would be interesting to examine the reduction of the electric and magnetic SE of non-spherical hollow CFC shells at their resonance frequencies e.g., inside an aircraft fuel tank. Furthermore, it would be worthwhile to calculate the interference that is

caused by a transmitter operated by a passenger inside the aircraft on the antennas that are mounted on the aircraft fuselage using the inside-outside formulation.

Modeling CFC materials in SE calculations has proved to be a challenge due to their moderate conductivity of $\sigma = 10^4$ S/m. This work was an effort on identifying key issues in modeling CFC materials in commercially available MoM-solvers. It is hoped that future researchers and practicing engineers find this thesis useful in their carrier.

Bibliography

[1] C. L. Holloway, M. S. Sarto, and M. Johansson, "Analyzing carbon-fiber composite materials with equivalent-layer models," *Electromagnetic Compatibility, IEEE Transactions on*, vol. 47, no. 4, pp. 833–844, 2005.

[2] M. Kimmel and H. Singer, "Numerical computation of anisotropic shielding materials based on the method of moments," in *Electromagnetic Compatibility, 1996. Symposium Record. IEEE 1996 International Symposium on*, 1996, pp. 87–91.

[3] D. A. Hill and J. R. Wait, "Electromagnetic scattering of an arbitrary plane wave by two nonintersecting perpendicular wire grids," *Can. J. Phys.*, vol. 52, no. 3, pp. 277–237, 1974.

[4] C. R. Paul, *Electromagnetic Compatibility*, 2nd ed. Wiley Online Library, 2006.

[5] EMSS, *How to increase the "dynamic range" of shielding problems in FEKO*. 100 Exploration Way, Suite 310-B, Hampton VA 23666, USA: FEKO Application Note, 2011.

[6] E. Guizzo, "Carbon takeoff [carbon fiber composites]," *Spectrum, IEEE*, vol. 43, no. 1, pp. 26–29, 2006.

[7] P. Mallick, *Fiber-Reinforced Composites: Materials, Manufacturing, and Design*, 3rd ed. CRC Press LLC, 2007.

[8] EMSS, *FEKO Suite 6.2*. 100 Exploration Way, Suite 310-B, Hampton VA 23666: EM Software & Systems-S.A. (Pty) Ltd. (EMSS-SA), 2012. [Online]. Available: www.feko.info

[9] M. J. Beran and N. R. Silnutzer, "Effective electrical, thermal and magnetic properties of fiber reinforced materials," *Journal of Composite Materials*, vol. 5, no. 2, pp. 246–249, 1971.

[10] F. Fisher and W. Fassell, "Lightning effects relating to aircraft. part i. lightning effects on and electromagnetic shielding properties of boron and graphite reinforced composite materials." DTIC Document, Tech. Rep., 1972.

[11] R. Knibbs and J. Morris, "The effects of fibre orientation on the physical properties of composites," *Composites*, vol. 5, no. 5, pp. 209–218, 1974.

[12] K. Keen, "Gain-loss measurements on a carbon-fibre composite reflector antenna," *Electronics Letters*, vol. 11, no. 11, pp. 234–235, 1975.

[13] ——, "Surface efficiency measurements on a high-modulus carbon fibre composite reflector antenna at l-and s-band frequencies," *Electronics Letters*, vol. 12, no. 7, pp. 160–161, 1976.

[14] C. Blake, "Composites-their electrical and electromagnetic impact," in *International Symposium on Electromagnetic Compatibility*, Washington, D.C; United States, July 1976.

[15] K. Casey, *Electromagnetic shielding by advanced composite materials*. Defense Technical Information Center, 1978.

[16] G. Weinstock, "Electromagnetic integration of composite structure in aircraft," in *NATO Advisory Group for Aerospace Research and Development, Avionics Panel, Conference*, no. 283. DTIC Document, 1980.

[17] D. Hill and J. Wait, "Analyses of electromagnetic scattering from wire-mesh structures," *Electronics Letters*, vol. 12, no. 17, pp. 427–428, 1976.

[18] P. Kazerani, "Analysis of antennas on carbon-fiber composite aircraft," Master's thesis, Concordia University, 2012.

[19] A. Mehdipour, "Advanced carbon fiber composite materials for shielding and antenna applications," Ph.D. dissertation, Concordia University, 2011.

[20] A. Mehdipour, I. Rosca, C. Trueman, A. Sebak, and S. V. Hoa, "Multiwall carbon nanotube-epoxy composites with high shielding effectiveness for aeronautic applications," *Electromagnetic Compatibility, IEEE Transactions on*, vol. 54, no. 1, pp. 28–36, 2012.

[21] F. A. Fisher and J. A. Plumer, *Lightning Protection of Aircraft*, 2nd ed. Lightning Technologies, 2004.

[22] L. Allen, W. F. Walker, and K. R. Siarkiewicz, "An investigation of the electromagnetic properties of advanced composite materials (in aircraft applications)," *International Symposium on Electromagnetic Compatibility*, pp. 174–179, July 1976.

[23] EMSS, *The effect of carbon fiber body panels on aircraft RCS*, FEKO Quarterly March 2010. [Online]. Available: http://www.feko.info/about-us/quarterly/feko-quarterly-march-2010

[24] D. A. Hill and J. R. Wait, "Electromagnetic scattering from an unbonded retangular wire mesh located near the air-ground interface," *Electromagnetic Compatibility, IEEE Transactions on*, vol. EMC-19, no. 4, pp. 402–406, 1977.

[25] ——, "Electromagnetic scattering of an arbitrary plane wave by a wire mesh with bonded junctions," *Canadian Journal of Physics*, vol. 54, no. 4, pp. 353–361, 1976.

[26] D. Hill and J. Wait, "Theoretical and numerical studies of wire mesh structures," Sensor and Simulation Note 231, Tech. Rep., June 1977.

[27] M. Ansarizadeh, A. Ozturk, and R. Paknys, "Using feko for electromagnetic analysis of carbon-fiber composite structures," in *27th Annual Review of Progress*

in Applied Computational Electromagnetics, March 27-31, 2011 - Williamsburg, VA, USA, pp. 353–356.

[28] A. Adams, W. Gajda, R. Heintz, W. Walker, and R. F. Stratton, "Electromagnetic properties and effects of advanced composite materials: Measurement and modeling," DTIC Document, Tech. Rep., 1978.

[29] W. Gajda, "A fundamental study of the electromagnetic properties of advanced composite materials," DTIC Document, Tech. Rep. RADC-TR-76-168, 1978.

[30] E. Newman and M. Schrote, "An open surface integral formulation for electromagnetic scattering by material plates," *Antennas and Propagation, IEEE Transactions on*, vol. 32, no. 7, pp. 672–678, 1984.

[31] EMSS, *FEKO Short Course Notes*, 100 Exploration Way, Suite 310-B, Hampton VA 23666, USA, 2010.

[32] ——, *FEKO 6.2 User's Manual*, September 2012.

[33] HFSS, *Version 15.0.0*. 275 Technology Drive, Canonsburg, PA 15317, USA: ANSYS, Inc., 2013. [Online]. Available: www.ansys.com

[34] L. Josefsson and P. Persson, *Conformal array antenna theory and design*. Wiley-IEEE Press, 2006, vol. 29.

[35] M. Ansarizadeh and R. Paknys, "Performance of monopole antennas on carbon fiber composite ground planes– theory and experiment," in *Canadian Aeronautics and Space Institute*, Montreal QC, Apr. 26-28, 2011.

[36] C. A. Balanis, *Advanced engineering electromagnetics*, 2nd ed. Wiley New York, 2012.

[37] Allred & Associates Inc., http://www.dragonplate.com., 321 Route 5 West, Elbridge, New York 13060, USA, 2013.

[38] E. J. Barbero, P. Lonetti, and K. K. Sikkil, "Finite element continuum damage modeling of plain weave reinforced composites," *Composites Part B: Engineering*, vol. 37, no. 2-3, pp. 137–147, 2005.

[39] *CST Studio Suite 2013*. CST-Computer Simulation Technology AG, 2012.

[40] R. Paknys, *Advanced Electromagnetics*. ELEC 6301 Course Notes, Concordia University, Montreal, QC, Canada, 2011.

[41] EMSS, "Feko examples guide," Dec. 2011, suite 6.1.1.

[42] J. R. Mautz and R. F. Harrington, "Electromagnetic scattering from a homogeneous material body of revolution," *Archiv Elektronik und Uebertragungstechnik*, vol. 33, pp. 71–80, 1979.

[43] Y.-H. Chu and W. C. Chew, "A robust surface-integral-equation formulation for conductive media," *Microwave and optical technology letters*, vol. 46, no. 2, pp. 109–114, 2005.

[44] A. L. Aden and M. Kerker, "Scattering of electromagnetic waves from two concentric spheres," *Journal of Applied Physics*, vol. 22, no. 10, pp. 1242–1246, 1951.

[45] R. F. Harrington, *Time-Harmonic Electromagnetic Fields*. IEEE Press, 2001.

[46] M. E. Abramowitz and I. Stegun, *Handbook of mathematical functions: with formulas, graphs, and mathematical tables*. Courier Dover Publications, 1964, vol. 55.

[47] R. L. Burden and J. D. Faires, *Numerical analysis*. Brooks/Cole, USA, 2001.

[48] MATLAB, *version 8.1.0.604 (R2013a)*. Natick, Massachusetts: The MathWorks Inc., 2013.

Appendix A

SE Inside a Hollow Spherical CFC Shell

A.1 Formulating the Problem

In this appendix, the analytic expression for the EM fields that leak through a hollow spherical shell are derived and a method is proposed to overcome the numerical problems that occur in the analytic solution when the shell's material is CFC. Fig. A.1 shows the cross section of a hollow spherical CFC shell which is illuminated by a plane wave. With reference to Fig. A.1, a and b represent the inner and outer radii of the shell, respectively. Furthermore, the subscripts 1, 2, and 3 represent the regions corresponding to $r \leq a$, $a \leq r \leq b$, and $r \geq b$, respectively. The electric and magnetic fields associated with the incident plane wave are, respectively, given by

$$\mathbf{E}^i = \hat{\mathbf{x}} E_x^i = \hat{\mathbf{x}} e^{-jk_3 z} \tag{A.1}$$

and

$$\mathbf{H}^i = \hat{\mathbf{y}} H_y^i = \hat{\mathbf{y}} \frac{1}{\eta_3} e^{-jk_3 z} \tag{A.2}$$

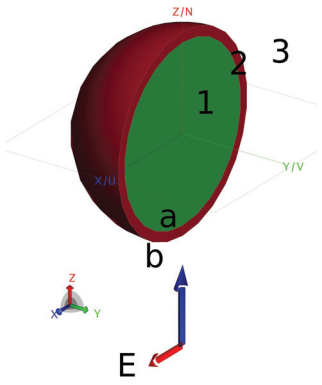

Figure A.1: The cross section of a hollow spherical CFC shell which is illuminated by a plane wave. a and b represent the inner and outer radii of the shell, respectively. The subscripts 1, 2, and 3, respectively, represent the regions corresponding to $r \leq a$, $a \leq r \leq b$, and $r \geq b$.

where k_3 and η_3 are, respectively, the wavenumber and impedance of the incident plane wave. In order to calculate the electric and magnetic fields that leak into the shell the spherical coordinate system and the concept of electric and magnetic vector potentials are employed [45]. The analytic solution is obtained by finding sets of spherical wave functions that satisfy the boundary conditions at $r = a$ and $r = b$. The boundary conditions are the continuity of the tangential electric and magnetic fields at $r = a$ and $r = b$. To satisfy the boundary conditions, it is necessary and sufficient to include TM^r and TE^r modes which are specified by the vector potentials $\mathbf{A} = \hat{\mathbf{r}}A_r$ and $\mathbf{F} = \hat{\mathbf{r}}F_r$, respectively. In the spherical coordinate system A_r/r and F_r/r satisfy the following scalar Helmholtz equations [45]:

$$(\nabla^2 + k^2)\frac{A_r}{r} = 0, \tag{A.3}$$

$$(\nabla^2 + k^2)\frac{F_r}{r} = 0 \tag{A.4}$$

where k is the wavenumber. Therefore, the electric and magnetic vector potentials everywhere in space should be expressed in terms of spherical wave functions that satisfy (A.3) or (A.4) and the boundary conditions. The electric and magnetic vector potentials in regions 1, 2, and 3 are written as follows.

For region 1 i.e., $0 \leq r \leq a$ we have:

$$A_r^1 = \frac{\cos\phi}{\omega\mu_1}\sum_{n=1}^{\infty} j^{-n}\frac{2n+1}{n(n+1)}a_n\hat{J}_n(k_1r)P_n^1(\cos\theta), \tag{A.5}$$

$$F_r^1 = \frac{\sin\phi}{k_1}\sum_{n=1}^{\infty} j^{-n}\frac{2n+1}{n(n+1)}b_n\hat{J}_n(k_1r)P_n^1(\cos\theta). \tag{A.6}$$

For region 2 i.e., $a \leq r \leq b$ we have:

$$A_r^2 = \frac{\cos\phi}{\omega\mu_2}\sum_{n=1}^{\infty} j^{-n}\frac{2n+1}{n(n+1)}\left[c_n\hat{J}_n(k_2r) + d_n\hat{N}_n(k_2r)\right]P_n^1(\cos\theta), \tag{A.7}$$

$$F_r^2 = \frac{\sin\phi}{k_2}\sum_{n=1}^{\infty} j^{-n}\frac{2n+1}{n(n+1)}\left[e_n\hat{J}_n(k_2r) + f_n\hat{N}_n(k_2r)\right]P_n^1(\cos\theta). \tag{A.8}$$

For region 3 i.e., $r \geq b$ we have:

$$A_r^3 = \frac{\cos\phi}{\omega\mu_3}\sum_{n=1}^{\infty} j^{-n}\frac{2n+1}{n(n+1)}\left[\hat{J}_n(k_3r) + g_n\hat{H}_n^{(2)}(k_3r)\right]P_n^1(\cos\theta), \tag{A.9}$$

$$F_r^3 = \frac{\sin\phi}{k_3}\sum_{n=1}^{\infty} j^{-n}\frac{2n+1}{n(n+1)}\left[\hat{J}_n(k_3r) + h_n\hat{H}_n^{(2)}(k_3r)\right]P_n^1(\cos\theta). \tag{A.10}$$

In (A.5)-(A.10) μ_i is the permeability of region i, $k_i = \omega\sqrt{\mu_i\epsilon_i}$ is the propagation constant in region i, and ϵ_i is the complex permittivity of region i. In (A.9) and (A.10), the incident plane wave is expressed in terms of spherical wave functions as [45]:

$$A_r^i = \frac{\cos\phi}{\omega\mu_3}\sum_{n=1}^{\infty} j^{-n}\frac{2n+1}{n(n+1)}\hat{J}_n(k_3r)P_n^1(\cos\theta), \tag{A.11}$$

$$F_r^i = \frac{\sin\phi}{k_3}\sum_{n=1}^{\infty} j^{-n}\frac{2n+1}{n(n+1)}\hat{J}_n(k_3r)P_n^1(\cos\theta). \tag{A.12}$$

where $P_n^1(\cos\theta)$ is the associated legendre function of degree n and order 1. Furthermore, in (A.5)-(A.12) $\hat{J}_n(.)$ and $\hat{N}_n(.)$ are the Schelkunoff Bessel functions of the first and second kind and integer order n which can be expressed as [45, 46]

$$\hat{J}_n(z) = z\left[f_n(z)\sin z + (-1)^{n+1}f_{-n-1}(z)\cos z\right] \tag{A.13}$$

and

$$\hat{N}_n(z) = z\left[-f_n(z)\cos z + (-1)^{n+1} f_{-n-1}(z)\sin z\right] \tag{A.14}$$

where

$$\begin{aligned} f_0(z) &= \tfrac{1}{z} \\ f_1(z) &= \tfrac{1}{z^2} \\ f_{n-1}(z) + f_{n+1}(z) &= (2n+1)\tfrac{f_n(z)}{z} \end{aligned} \quad . \tag{A.15}$$

Furthermore, $\hat{H}_n^{(2)}(.) = \hat{J}_n(.) - j\hat{N}_n(.)$.

By calculating the unknown coefficients a_n, b_n, c_n, d_n, e_n, f_n, g_n, and h_n in (A.5)-(A.10) the vector potentials everywhere in space can be obtained. a_n, b_n,...,h_n are found such that the boundary conditions at $r = a$, and $r = b$ are satisfied. Since there are no impressed surface currents at $r = a$ and $r = b$ the tangential components of the electric and magnetic fields (E_θ, H_θ, E_ϕ, and H_ϕ) are continuous at $r = a$ and $r = b$. The tangential fields at $r = a^-$, $r = b^-$, $r = a^+$, and $r = b^+$ can be obtained from (A.5)-(A.10) by using the following equations [45]:

$$E_\theta^i = \frac{-1}{r\sin\theta}\frac{\partial F_r^i}{\partial\phi} + \frac{1}{j\omega\epsilon_i}\frac{\partial^2 A_r^i}{r\partial r\partial\theta}, \tag{A.16}$$

$$E_\phi^i = \frac{1}{r}\frac{\partial F_r^i}{\partial\theta} + \frac{1}{j\omega\epsilon_i}\frac{1}{r\sin\theta}\frac{\partial^2 A_r^i}{\partial r\partial\phi}, \tag{A.17}$$

$$H_\theta^i = \frac{1}{r\sin\theta}\frac{\partial A_r^i}{\partial\phi} + \frac{1}{j\omega\mu_i}\frac{\partial^2 F_r^i}{r\partial r\partial\theta}, \tag{A.18}$$

and

$$H_\phi^i = \frac{1}{r}\frac{\partial F_r^i}{\partial\theta} + \frac{1}{j\omega\epsilon_i}\frac{1}{r\sin\theta}\frac{\partial^2 A_r^i}{\partial r\partial\phi} \tag{A.19}$$

where i denotes the region in which fields are evaluated. Using (A.5), (A.6), and (A.16), E_θ in region 1 at $r = a^-$ and E_θ in region 2 at $r = a^+$ can be written as:

$$\begin{aligned} E_\theta^1|_{r=a^-} = &-\cos\phi\sum_{n=1}^{\infty} j^{-n}\frac{2n+1}{n(n+1)}b_n\frac{\hat{J}_n(k_1a)}{k_1a}\frac{P_n^1(\cos\theta)}{\sin\theta} + \\ &-j\cos\phi\sum_{n=1}^{\infty} j^{-n}\frac{2n+1}{n(n+1)}a_n\frac{\hat{J}_n'(k_1a)}{k_1a}\frac{\partial P_n^1(\cos\theta)}{\partial\theta} \end{aligned} \tag{A.20}$$

and

$$E_\theta^2|_{r=a^+} = -\cos\phi \sum_{n=1}^{\infty} j^{-n} \frac{2n+1}{n(n+1)} \left[e_n \frac{\hat{J}_n(k_2 a)}{k_2 a} + f_n \frac{\hat{N}_n(k_2 a)}{k_2 a} \right] \frac{P_n^1(\cos\theta)}{\sin\theta} + \\ -j\cos\phi \sum_{n=1}^{\infty} j^{-n} \frac{2n+1}{n(n+1)} \left[c_n \frac{\hat{J}_n'(k_2 a)}{k_2 a} + d_n \frac{\hat{N}_n'(k_2 a)}{k_2 a} \right] \frac{\partial P_n^1(\cos\theta)}{\partial\theta}. \tag{A.21}$$

By imposing the boundary condition that $E_\theta^1|_{r=a^-} = E_\theta^2|_{r=a^+}$ the following equations are obtained:

$$a_n \frac{\hat{J}_n'(k_1 a)}{k_1 a} - c_n \frac{\hat{J}_n'(k_2 a)}{k_2 a} - d_n \frac{\hat{N}_n'(k_2 a)}{k_2 a} = 0 \tag{A.22}$$

and

$$b_n \frac{\hat{J}_n(k_1 a)}{k_1 a} - e_n \frac{\hat{J}_n(k_2 a)}{k_2 a} - f_n \frac{\hat{N}_n(k_2 a)}{k_2 a} = 0. \tag{A.23}$$

It is worth noting that conditions that make E_θ continuous at $r = a$ or $r = b$ also make E_ϕ continuous at $r = a$ or $r = b$. This conclusion can be extended to magnetic fields, also. Using (A.5), (A.6), and (A.18) the magnetic fields in region 1 at $r = a^-$ and in region 2 at $r = a^+$ are written as

$$H_\theta^1|_{r=a^-} = -\frac{\sin\phi}{\eta_1} \sum_{n=1}^{\infty} j^{-n} \frac{2n+1}{n(n+1)} a_n \frac{\hat{J}_n(k_1 a)}{k_1 a} \frac{P_n^1(\cos\theta)}{\sin\theta} + \\ \frac{\sin\phi}{j\eta_1} \sum_{n=1}^{\infty} j^{-n} \frac{2n+1}{n(n+1)} b_n \frac{\hat{J}_n'(k_1 a)}{k_1 a} \frac{\partial P_n^1(\cos\theta)}{\partial\theta} \tag{A.24}$$

and

$$H_\theta^2|_{r=a^+} = -\frac{\sin\phi}{\eta_2} \sum_{n=1}^{\infty} j^{-n} \frac{2n+1}{n(n+1)} \left[c_n \frac{\hat{J}_n(k_2 a)}{k_2 a} + d_n \frac{\hat{N}_n(k_2 a)}{k_2 a} \right] \frac{P_n^1(\cos\theta)}{\sin\theta} + \\ \frac{\sin\phi}{j\eta_2} \sum_{n=1}^{\infty} j^{-n} \frac{2n+1}{n(n+1)} \left[e_n \frac{\hat{J}_n'(k_2 a)}{k_2 a} + f_n \frac{\hat{N}_n'(k_2 a)}{k_2 a} \right] \frac{\partial P_n^1(\cos\theta)}{\partial\theta}. \tag{A.25}$$

Imposing the boundary condition that $H_\theta^1|_{r=a^-} = H_\theta^2|_{r=a^+}$ lead to

$$a_n \frac{\hat{J}_n(k_1 a)}{\eta_1 k_1 a} - c_n \frac{\hat{J}_n(k_2 a)}{\eta_2 k_2 a} - d_n \frac{\hat{N}_n(k_2 a)}{\eta_2 k_2 a} = 0 \tag{A.26}$$

and

$$b_n \frac{\hat{J}_n'(k_1 a)}{\eta_1 k_1 a} - e_n \frac{\hat{J}_n'(k_2 a)}{\eta_2 k_2 a} - f_n \frac{\hat{N}_n'(k_2 a)}{\eta_2 k_2 a} = 0. \tag{A.27}$$

Using (A.7), (A.8), and (A.16) E_θ in region 1 at $r = b^-$ and E_θ in region 2 at $r = b^+$ can be written as

$$\begin{aligned} E_\theta^2|_{r=b^-} = &- \cos\phi \sum_{n=1}^{\infty} j^{-n} \frac{2n+1}{n(n+1)} \left[e_n \frac{\hat{J}_n(k_2 b)}{k_2 b} + f_n \frac{\hat{N}_n(k_2 b)}{k_2 b} \right] \frac{P_n^1(\cos\theta)}{\sin\theta} + \\ &- j \cos\phi \sum_{n=1}^{\infty} j^{-n} \frac{2n+1}{n(n+1)} \left[c_n \frac{\hat{J}_n'(k_2 b)}{k_2 b} + d_n \frac{\hat{N}_n'(k_2 b)}{k_2 b} \right] \frac{\partial P_n^1(\cos\theta)}{\partial\theta} \end{aligned} \tag{A.28}$$

and

$$\begin{aligned} E_\theta^3|_{r=b^+} = &- \cos\phi \sum_{n=1}^{\infty} j^{-n} \frac{2n+1}{n(n+1)} \left[\frac{\hat{J}_n(k_3 b)}{k_3 b} + h_n \frac{\hat{H}_n^{(2)}(k_3 b)}{k_3 b} \right] \frac{P_n^1(\cos\theta)}{\sin\theta} + \\ &- j \cos\phi \sum_{n=1}^{\infty} j^{-n} \frac{2n+1}{n(n+1)} \left[\frac{\hat{J}_n'(k_3 b)}{k_3 b} + g_n \frac{\hat{H}_n^{(2)'}(k_3 b)}{k_3 b} \right] \frac{\partial P_n^1(\cos\theta)}{\partial\theta}. \end{aligned} \tag{A.29}$$

The boundary conditions associated with the continuity of the electric fields at $r = b$ lead to

$$c_n \frac{\hat{J}_n'(k_2 b)}{k_2 b} + d_n \frac{\hat{N}_n'(k_2 b)}{k_2 b} - g_n \frac{\hat{H}_n^{(2)\prime}(k_3 b)}{k_3 b} - \frac{\hat{J}_n'(k_3 b)}{k_3 b} = 0 \tag{A.30}$$

and

$$e_n \frac{\hat{J}_n(k_2 b)}{k_2 b} + f_n \frac{\hat{N}_n(k_2 b)}{k_2 b} - h_n \frac{\hat{H}_n^{(2)}(k_3 b)}{k_3 b} - \frac{\hat{J}_n'(k_3 b)}{k_3 b} = 0. \tag{A.31}$$

Using (A.7)-(A.10), and (A.18) the magnetic fields at $r = b^-$ and $r = b^+$ can be written as

$$\begin{aligned} H_\theta^2|_{r=b^-} = &- \frac{\sin\phi}{\eta_2} \sum_{n=1}^{\infty} j^{-n} \frac{2n+1}{n(n+1)} \left[c_n \frac{\hat{J}_n(k_2 b)}{k_2 b} + d_n \frac{\hat{N}_n(k_2 b)}{k_2 b} \right] \frac{P_n^1(\cos\theta)}{\sin\theta} + \\ &\frac{\sin\phi}{j\eta_2} \sum_{n=1}^{\infty} j^{-n} \frac{2n+1}{n(n+1)} \left[e_n \frac{\hat{J}_n'(k_2 b)}{k_2 b} + f_n \frac{\hat{N}_n'(k_2 b)}{k_2 b} \right] \frac{\partial P_n^1(\cos\theta)}{\partial\theta} \end{aligned} \tag{A.32}$$

and

$$H_\theta^3|_{r=b^+} = -\frac{\sin\phi}{\eta_3}\sum_{n=1}^{\infty} j^{-n}\frac{2n+1}{n(n+1)}\left[\frac{\hat{J}_n(k_3b)}{k_3b} + g_n\frac{\hat{H}_n^{(2)}(k_3b)}{k_3b}\right]\frac{P_n^1(\cos\theta)}{\sin\theta} + \frac{\sin\phi}{j\eta_3}\sum_{n=1}^{\infty} j^{-n}\frac{2n+1}{n(n+1)}\left[\frac{\hat{J}_n'(k_3b)}{k_3b} + h_n\frac{\hat{H}_n^{(2)'}(k_3b)}{k_3b}\right]\frac{\partial P_n^1(\cos\theta)}{\partial\theta}. \tag{A.33}$$

The boundary conditions associated with the continuity of the magnetic fields at $r = b$ lead to

$$c_n\frac{\hat{J}_n(k_2b)}{\eta_2k_2b} + d_n\frac{\hat{N}_n(k_2b)}{\eta_2k_2b} - g_n\frac{\hat{H}_n^{(2)}(k_3b)}{\eta_3k_3b} - \frac{\hat{J}_n(k_3b)}{\eta_3k_3b} = 0 \tag{A.34}$$

and

$$e_n\frac{\hat{J}_n'(k_2b)}{\eta_2k_2b} + f_n\frac{\hat{N}_n'(k_2b)}{\eta_2k_2b} - h_n\frac{\hat{H}_n^{(2)\prime}(k_3b)}{\eta_3k_3b} - \frac{\hat{J}_n'(k_3b)}{\eta_3k_3b} = 0. \tag{A.35}$$

Now that the boundary conditions are imposed the eight unknown coefficients a_n,...,h_n may be determined. In the matrix form (A.22), (A.23), (A.26), (A.27), (A.30), (A.31), (A.34), and (A.35) can be written as

$$\begin{bmatrix} \frac{\hat{J}_n'(k_1a)}{k_1a} & \frac{-\hat{J}_n'(k_2a)}{k_2a} & \frac{-\hat{N}_n'(k_2a)}{k_2a} & 0 \\ \frac{\hat{J}_n(k_1a)}{\eta_1k_1a} & \frac{-\hat{J}_n(k_2a)}{\eta_2k_2a} & \frac{-\hat{N}_n(k_2a)}{\eta_2k_2b} & 0 \\ 0 & \frac{\hat{J}_n'(k_2b)}{k_2b} & \frac{\hat{N}_n'(k_2b)}{k_2b} & \frac{-\hat{H}_n^{(2)\prime}(k_3b)}{k_3b} \\ 0 & \frac{\hat{J}_n(k_2b)}{\eta_2k_2b} & \frac{\hat{N}_n(k_2b)}{\eta_2k_2b} & \frac{-\hat{H}_n^{(2)}(k_3b)}{\eta_3k_3b} \end{bmatrix}\begin{bmatrix} a_n \\ c_n \\ d_n \\ g_n \end{bmatrix} = \begin{bmatrix} 0 \\ 0 \\ \frac{\hat{J}_n'(k_3b)}{k_3b} \\ \frac{\hat{J}_n(k_3b)}{\eta_3k_3b} \end{bmatrix} \tag{A.36}$$

and

$$\begin{bmatrix} \frac{\hat{J}_n(k_1a)}{k_1a} & \frac{-\hat{J}_n(k_2a)}{k_2a} & \frac{-\hat{N}_n(k_2a)}{k_2a} & 0 \\ \frac{\hat{J}_n'(k_1a)}{\eta_1k_1a} & \frac{-\hat{J}_n'(k_2a)}{\eta_2k_2a} & \frac{-\hat{N}_n'(k_2a)}{\eta_2k_2a} & 0 \\ 0 & \frac{\hat{J}_n(k_2b)}{k_2b} & \frac{\hat{N}_n(k_2b)}{k_2b} & \frac{-\hat{H}_n^{(2)}(k_3b)}{k_3b} \\ 0 & \frac{\hat{J}_n'(k_2b)}{\eta_2k_2b} & \frac{\hat{N}_n'(k_2b)}{\eta_2k_2b} & \frac{-\hat{H}_n^{(2)\prime}(k_3b)}{\eta_3k_3a} \end{bmatrix}\begin{bmatrix} b_n \\ e_n \\ f_n \\ h_n \end{bmatrix} = \begin{bmatrix} 0 \\ 0 \\ \frac{\hat{J}_n(k_3b)}{k_3b} \\ \frac{\hat{J}_n'(k_3b)}{\eta_3k_3a} \end{bmatrix}. \tag{A.37}$$

Eqs. (A.36) and (A.37) may be solved using the standard numerical methods for solving linear systems [47]. Then, the electric and magnetic fields that leak through the shell to the region of $r \leq a$ can be expressed using (A.5), (A.6), and the following

equations [45]:

$$E_r^1 = \frac{1}{j\omega\epsilon_1}(k_1^2 + \frac{\partial^2}{\partial r^2})A_r^1 = -j\cos\phi\sum_{n=1}^{\infty} j^{-n}\frac{2n+1}{n(n+1)}a_n\left[\hat{J}_n(k_1r) + \hat{J}_n''(k_1r)\right]P_n^1(\cos\theta), \tag{A.38}$$

$$\begin{aligned} E_\theta^1 = \frac{-1}{r\sin\theta}\frac{\partial F_r^1}{\partial\phi} + \frac{1}{j\omega\epsilon_1}\frac{\partial^2 A_r^1}{r\partial r\partial\theta} = &-\cos\phi\sum_{n=1}^{\infty} j^{-n}\frac{2n+1}{n(n+1)}b_n\frac{\hat{J}_n(k_1r)}{k_1r}\frac{P_n^1(\cos\theta)}{\sin\theta} \\ &-j\cos\phi\sum_{n=1}^{\infty} j^{-n}\frac{2n+1}{n(n+1)}a_n\frac{\hat{J}_n'(k_1r)}{k_1r}\frac{\partial P_n^1(\cos\theta)}{\partial\theta}, \end{aligned} \tag{A.39}$$

$$\begin{aligned} E_\phi^1 = \frac{1}{r}\frac{\partial F_r^1}{\partial\theta} + \frac{1}{j\omega\epsilon_1}\frac{1}{r\sin\theta}\frac{\partial^2 A_r^1}{\partial r\partial\phi} = &\sin\phi\sum_{n=1}^{\infty} j^{-n}\frac{2n+1}{n(n+1)}b_n\frac{\hat{J}_n(k_1r)}{k_1r}\frac{\partial P_n^1(\cos\theta)}{\partial\theta} \\ &+j\sin\phi\sum_{n=1}^{\infty} j^{-n}\frac{2n+1}{n(n+1)}a_n\frac{\hat{J}_n'(k_1r)}{k_1r}\frac{P_n^1(\cos\theta)}{\sin\theta}, \end{aligned} \tag{A.40}$$

$$H_r^1 = \frac{1}{j\omega\mu_1}(k_1^2 + \frac{\partial^2}{\partial r^2})F_r^1 = \frac{1}{j\eta_1}\sin\phi\sum_{n=1}^{\infty} j^{-n}\frac{2n+1}{n(n+1)}b_n\left[\hat{J}_n(k_1r) + \hat{J}_n''(k_1r)\right]P_n^1(\cos\theta), \tag{A.41}$$

$$\begin{aligned} H_\theta^1 = \frac{1}{r\sin\theta}\frac{\partial A_r^1}{\partial\phi} + \frac{1}{j\omega\mu_1}\frac{\partial^2 F_r^1}{r\partial r\partial\theta} = &-\frac{\sin\phi}{\eta_1}\sum_{n=1}^{\infty} j^{-n}\frac{2n+1}{n(n+1)}a_n\frac{\hat{J}_n(k_1r)}{k_1r}\frac{P_n^1(\cos\theta)}{\sin\theta} \\ &+\frac{\sin\phi}{j\eta_1}\sum_{n=1}^{\infty} j^{-n}\frac{2n+1}{n(n+1)}b_n\frac{\hat{J}_n'(k_1r)}{k_1r}\frac{\partial P_n^1(\cos\theta)}{\partial\theta}, \end{aligned} \tag{A.42}$$

and

$$\begin{aligned} H_\phi^1 = \frac{1}{r}\frac{\partial F_r^1}{\partial\theta} + \frac{1}{j\omega\epsilon_1}\frac{1}{r\sin\theta}\frac{\partial^2 A_r^1}{\partial r\partial\phi} = &\frac{-\cos\phi}{\eta_1}\sum_{n=1}^{\infty} j^{-n}\frac{2n+1}{n(n+1)}b_n\frac{\hat{J}_n(k_1r)}{k_1r}\frac{\partial P_n^1(\cos\theta)}{\partial\theta} \\ &+\frac{\cos\phi}{j\eta_1}\sum_{n=1}^{\infty} j^{-n}\frac{2n+1}{n(n+1)}a_n\frac{\hat{J}_n'(k_1r)}{k_1r}\frac{P_n^1(\cos\theta)}{\sin\theta}. \end{aligned} \tag{A.43}$$

A.2 Fields at the Origin

Eqs. (A.38)-(A.43) may be used to calculate fields everywhere inside the shell. The fields at the origin can be found using only the terms a_1 and b_1. Using (A.38)-(A.43) the magnitude of the electric and magnetic fields at the origin are, respectively

$$\lim_{r\to 0}|\mathbf{E}^1(r,\theta,\phi)| = \sqrt{|E_r^1|^2+|E_\theta^1|^2+|E_\phi^1|^2} = |a_1| \tag{A.44}$$

and

$$\lim_{r\to 0}|\mathbf{H}^1(r,\theta,\phi)| = \sqrt{|H_r^1|^2+|H_\theta^1|^2+|H_\phi^1|^2} = \frac{|b_1|}{\eta_0}. \tag{A.45}$$

To obtain (A.44) and (A.45) use has been made of the following limitations and identities [46]:

$$\lim_{r\to 0}\frac{\hat{J}_n(k_1 r)}{k_1 r} = 0,\ n\geq 1, \tag{A.46}$$

$$\lim_{r\to 0}\frac{\hat{J}_n'(k_1 r)}{k_1 r} = \lim_{r\to 0}\hat{J}_n''(k_1 r) = \begin{cases} 2/3, & n=1 \\ 0, & n>1 \end{cases}, \tag{A.47}$$

$$P_1(\cos\theta) = \cos\theta, \tag{A.48}$$

and

$$P_1^1(\cos\theta) = \frac{\partial P_1(\cos\theta)}{\partial\theta} = -\sin\theta. \tag{A.49}$$

A.3 Numerical Issues

Fig. A.1 shows a hollow spherical CFC shell which is illuminated by a plane wave at the frequency of $f = 100$ MHz. The propagation constant in the CFC material with $\sigma = 10^4$ S/m is given by [36]

$$k_2 = \frac{\sqrt{j2\pi f\mu_0\sigma}}{j} = 1986.9 - j1986.9 \ \ [rad/m]. \tag{A.50}$$

Using (A.50), the Schelkunoff Bessel functions $\hat{J}_n(k_2b)$ and $\hat{N}_n(k_2b)$ which are given by (A.13)-(A.15) could not be evaluated for $b > 35$ cm even when double precision variable are employed. This is because $\sin(k_2b)$ and $\cos(k_2b)$ overflow for $b > 35$ cm. To eliminate this problem, a_n and b_n are expressed in terms of $\sin[k_2(b-a)]$ and $\cos[k_2(b-a)]$ as described in the following.

Using (A.36) and (A.37), a_n and b_n can be written as

$$a_n = \frac{\begin{vmatrix} 0 & \frac{-\hat{J}_n'(k_2a)}{k_2a} & \frac{-\hat{N}_n'(k_2a)}{k_2a} & 0 \\ 0 & \frac{-\hat{J}_n(k_2a)}{\eta_2 k_2a} & \frac{-\hat{N}_n(k_2a)}{\eta_2 k_2a} & 0 \\ \frac{\hat{J}_n'(k_3b)}{k_3b} & \frac{\hat{J}_n'(k_2b)}{k_2b} & \frac{\hat{N}_n'(k_2b)}{k_2b} & \frac{-\hat{H}_n^{(2)\prime}(k_3b)}{k_3b} \\ \frac{\hat{J}_n(k_3b)}{\eta_3 k_3b} & \frac{\hat{J}_n(k_2b)}{\eta_2 k_2b} & \frac{\hat{N}_n(k_2b)}{\eta_2 k_2b} & \frac{-\hat{H}_n^{(2)}(k_3b)}{\eta_3 k_3b} \end{vmatrix}}{\begin{vmatrix} \frac{\hat{J}_n'(k_1a)}{k_1a} & \frac{-\hat{J}_n'(k_2a)}{k_2a} & \frac{-\hat{N}_n'(k_2a)}{k_2a} & 0 \\ \frac{\hat{J}_n(k_1a)}{\eta_1 k_1a} & \frac{-\hat{J}_n(k_2a)}{\eta_2 k_2a} & \frac{-\hat{N}_n(k_2a)}{\eta_2 k_2a} & 0 \\ 0 & \frac{\hat{J}_n'(k_2b)}{k_2b} & \frac{\hat{N}_n'(k_2b)}{k_2b} & \frac{-\hat{H}_n^{(2)\prime}(k_3b)}{k_3b} \\ 0 & \frac{\hat{J}_n(k_2b)}{\eta_2 k_2b} & \frac{\hat{N}_n(k_2b)}{\eta_2 k_2b} & \frac{-\hat{H}_n^{(2)}(k_3b)}{\eta_3 k_3b} \end{vmatrix}} = \frac{\frac{1}{j\eta_2\eta_3(k_2ak_3b)^2}}{\Delta_n^{TM}} \tag{A.51}$$

and

$$b_n = \frac{\begin{vmatrix} 0 & \frac{-\hat{J}_n(k_2a)}{k_2a} & \frac{-\hat{N}_n(k_2a)}{k_2a} & 0 \\ 0 & \frac{-\hat{J}_n'(k_2a)}{\eta_2 k_2a} & \frac{-\hat{N}_n'(k_2a)}{\eta_2 k_2a} & 0 \\ \frac{\hat{J}_n(k_3b)}{k_3b} & \frac{\hat{J}_n(k_2b)}{k_2b} & \frac{\hat{N}_n(k_2b)}{k_2b} & \frac{-\hat{H}_n^{(2)}(k_3b)}{k_3b} \\ \frac{\hat{J}_n'(k_3b)}{\eta_3 k_3b} & \frac{\hat{J}_n'(k_2b)}{\eta_2 k_2b} & \frac{\hat{N}_n'(k_2b)}{\eta_2 k_2b} & \frac{-\hat{H}_n^{(2)\prime}(k_3b)}{\eta_3 k_3b} \end{vmatrix}}{\begin{vmatrix} \frac{\hat{J}_n(k_1a)}{k_1a} & \frac{-\hat{J}_n(k_2a)}{k_2a} & \frac{-\hat{N}_n(k_2a)}{k_2a} & 0 \\ \frac{\hat{J}_n'(k_1a)}{\eta_1 k_1a} & \frac{-\hat{J}_n'(k_2a)}{\eta_2 k_2a} & \frac{-\hat{N}_n'(k_2a)}{\eta_2 k_2a} & 0 \\ 0 & \frac{\hat{J}_n(k_2b)}{k_2b} & \frac{\hat{N}_n(k_2b)}{k_2b} & \frac{-\hat{H}_n^{(2)}(k_3b)}{k_3b} \\ 0 & \frac{\hat{J}_n'(k_2b)}{\eta_2 k_2b} & \frac{\hat{N}_n'(k_2b)}{\eta_2 k_2b} & \frac{-\hat{H}_n^{(2)\prime}(k_3b)}{\eta_3 k_3b} \end{vmatrix}} = \frac{\frac{j}{\eta_2\eta_3(k_2ak_3b)^2}}{\Delta_n^{TE}} \tag{A.52}$$

where

$$\begin{aligned}\Delta_n^{TM} = &-\frac{1}{\eta_1\eta_2 k_1 k_3 (k_2 ab)^2}\hat{J}_n(k_1a)\hat{H}_n^{(2)'}(k_3b)\left[\hat{J}_n(k_2b)\hat{N}_n'(k_2a) - \hat{N}_n(k_2b)\hat{J}_n'(k_2a)\right] \\ &-\frac{1}{\eta_1\eta_3 k_1 k_3 (k_2 ab)^2}\hat{J}_n(k_1a)\hat{H}_n^{(2)}(k_3b)\left[\hat{J}_n'(k_2a)\hat{N}_n'(k_2b) - \hat{N}_n'(k_2a)\hat{J}_n'(k_2b)\right] \\ &-\frac{1}{\eta_3\eta_2 k_1 k_3 (k_2 ab)^2}\hat{J}_n'(k_1a)\hat{H}_n^{(2)}(k_3b)\left[\hat{J}_n'(k_2b)\hat{N}_n(k_2a) - \hat{N}_n'(k_2b)\hat{J}_n(k_2a)\right] \\ &-\frac{1}{\eta_2^2 k_1 k_3 (k_2 ab)^2}\hat{J}_n'(k_1a)\hat{H}_n^{(2)'}(k_3b)\left[\hat{J}_n(k_2a)\hat{N}_n(k_2b) - \hat{N}_n(k_2a)\hat{J}_n(k_2b)\right],\end{aligned} \tag{A.53}$$

and

$$\begin{aligned}\Delta_n^{TE} = &-\frac{1}{\eta_2\eta_3 k_1 k_3 (k_2 ab)^2}\hat{J}_n(k_1a)\hat{H}_n^{(2)'}(k_3b)\left[\hat{J}_n(k_2b)\hat{N}_n'(k_2a) - \hat{N}_n(k_2b)\hat{J}_n'(k_2a)\right] \\ &-\frac{1}{\eta_2^2 k_1 k_3 (k_2 ab)^2}\hat{J}_n(k_1a)\hat{H}_n^{(2)}(k_3b)\left[\hat{J}_n'(k_2a)\hat{N}_n'(k_2b) - \hat{N}_n'(k_2a)\hat{J}_n'(k_2b)\right] \\ &-\frac{1}{\eta_1\eta_2 k_1 k_3 (k_2 ab)^2}\hat{J}_n'(k_1a)\hat{H}_n^{(2)}(k_3b)\left[\hat{J}_n'(k_2b)\hat{N}_n(k_2a) - \hat{N}_n'(k_2b)\hat{J}_n(k_2a)\right] \\ &-\frac{1}{\eta_1\eta_3 k_1 k_3 (k_2 ab)^2}\hat{J}_n'(k_1a)\hat{H}_n^{(2)'}(k_3b)\left[\hat{J}_n(k_2a)\hat{N}_n(k_2b) - \hat{N}_n(k_2a)\hat{J}_n(k_2b)\right].\end{aligned} \tag{A.54}$$

The numerators in (A.51) and (A.52) are simplified using

$$W(\hat{J}_n(k_3b), \hat{H}_n^{(2)}(k_3b)) = -j \tag{A.55}$$

and

$$W(\hat{J}_n(k_2a), \hat{N}_n(k_2a)) = 1 \tag{A.56}$$

where $W(.,.)$ is the Wronskian operator [45, 46]. In order to evaluate (A.53) and (A.54), the terms $\hat{J}_n(k_2a)$, $\hat{J}_n'(k_2a)$, $\hat{J}_n(k_2b)$, $\hat{J}_n'(k_2b)$, $\hat{N}_n(k_2a)$, $\hat{N}_n'(k_2a)$, $\hat{N}_n(k_2b)$, $\hat{N}_n'(k_2b)$ should not be evaluated individually. Instead the following equations should be used:

$$\hat{J}_n(k_2a)\hat{N}_n(k_2b) - \hat{N}_n(k_2a)\hat{J}_n(k_2b) = k_2^2 ab W_n^1(k_2a, k_2b), \tag{A.57}$$

$$\hat{J}'_n(k_2b)\hat{N}_n(k_2a) - \hat{N}'_n(k_2b)\hat{J}_n(k_2a) = -k_2aW^1_n(k_2a,k_2b) + k_2^2ab[W^2_n(k_2a,k_2b) + W^3_n(k_2a,k_2b)], \tag{A.58}$$

$$\hat{J}_n(k_2b)\hat{N}'_n(k_2a) - \hat{N}_n(k_2b)\hat{J}'_n(k_2a) = -k_2bW^1_n(k_2a,k_2b) + k_2^2ab[W^4_n(k_2a,k_2b) - W^3_n(k_2a,k_2b)], \tag{A.59}$$

and

$$\begin{aligned}\hat{J}'_n(k_2a)\hat{N}'_n(k_2b) - \hat{N}'_n(k_2a)\hat{J}'_n(k_2b) = W^1_n(k_2a,k_2b) + k_2^2ab[W^5_n(k_2a,k_2b) + \\ W^6_n(k_2a,k_2b) + W^1_n(k_2a,k_2b)] + k_2a\left[W^3_n(k_2a,k_2b) - W^4_n(k_2a,k_2b)\right] \\ -k_2b\left[W^2_n(k_2a,k_2b) + W^3_n(k_2a,k_2b)\right].\end{aligned} \tag{A.60}$$

Moreover, $W^1_n(k_2a,k_2b)$, $W^2_n(k_2a,k_2b)$,...,$W^6_n(k_2a,k_2b)$ are given by:

$$\begin{aligned}W^1_n(k_2a,k_2b) = (-1)^{n+1}\left[f_n(k_2a)f_{-n-1}(k_2b) - f_n(k_2b)f_{-n-1}(k_2a)\right]\cos(k_2b-k_2a) + \\ \left[f_n(k_2a)f_n(k_2b) + f_{-n-1}(k_2a)f_{-n-1}(k_2b)\right]\sin(k_2b-k_2a),\end{aligned} \tag{A.61}$$

$$\begin{aligned}W^2_n(k_2a,k_2b) = (-1)^{(n+1)}\left[f_{-n-1}(k_2a)f'_n(k_2b) - f_n(k_2a)f'_{-n-1}(k_2b)\right]\cos\left[k_2(b-a)\right] - \\ \left[f_{-n-1}(k_2a)f'_{-n-1}(k_2b) + f_n(k_2a)f'_n(k_2b)\right]\sin\left[k_2(b-a)\right],\end{aligned} \tag{A.62}$$

$$\begin{aligned}W^3_n(k_2a,k_2b) = (-1)^{(n+1)}\left[f_n(k_2a)f'_{-n-1}(k_2b) - f_n(k_2b)f'_{-n-1}(k_2a)\right]\sin\left[k_2(b-a)\right] - \\ \left[f_n(k_2a)f'_n(k_2b) + f_{-n-1}(k_2a)f_{-n-1}(k_2b)\right]\cos\left[k_2(b-a)\right],\end{aligned} \tag{A.63}$$

$$\begin{aligned}W^4_n(k_2a,k_2b) = (-1)^{n+1}\left[f'_{-n-1}(k_2a)f_n(k_2b) - f'_n(k_2a)f_{-n-1}(k_2b)\right]\cos\left[k_2(b-a)\right] - \\ \left[f'_{-n-1}(k_2a)f_{-n-1}(k_2b) + f'_n(k_2a)f_n(k_2b)\right]\sin\left[k_2(b-a)\right],\end{aligned} \tag{A.64}$$

$$\begin{aligned}W^5_n(k_2a,k_2b) = \left[f'_n(k_2a)f'_n(k_2b) + f'_{-n-1}(k_2a)f'_{-n-1}(k_2b)\right]\sin\left[k_2(b-a)\right] \\ +(-1)^{n+1}\left[f'_n(k_2a)f'_{-n-1}(k_2b) - f'_n(k_2b)f'_{-n-1}(k_2a)\right]\cos\left[k_2(b-a)\right],\end{aligned} \tag{A.65}$$

and

$$W_n^6(k_2a, k_2b) = \sin\left[k_2(b-a)\right](-1)^{n+1}[f_n(k_2a)f'_{-n-1}(k_2b) - f'_n(k_2a)f_{-n-1}(k_2b) - f_{-n-1}(k_2a)f'_n(k_2b) + f'_{-n-1}(k_2a)f_n(k_2b)] + \cos\left[k_2(b-a)\right][-f_n(k_2a)f'_n(k_2b) + fn'(k_2a)f_n(k_2b) - f_{-n-1}(k_2a)f'_{-n-1}(k_2b) + f'_{-n-1}(k_2a)f_{-n-1}(k_2b)]. \tag{A.66}$$

Eqs. (A.61)-(A.66) are obtained by replacing (A.13)-(A.15) in (A.53) and (A.54) and simplifying the resulting expressions using the symbolic math toolbox in MATLAB [48].